2D transition metal dichalcogenides

Sajedeh Manzeli[1,2], Dmitry Ovchinnikov[1,2], Diego Pasquier[3], Oleg V. Yazyev[3] and Andras Kis[1,2]

Abstract | Graphene is very popular because of its many fascinating properties, but its lack of an electronic bandgap has stimulated the search for 2D materials with semiconducting character. Transition metal dichalcogenides (TMDCs), which are semiconductors of the type MX_2, where M is a transition metal atom (such as Mo or W) and X is a chalcogen atom (such as S, Se or Te), provide a promising alternative. Because of its robustness, MoS_2 is the most studied material in this family. TMDCs exhibit a unique combination of atomic-scale thickness, direct bandgap, strong spin–orbit coupling and favourable electronic and mechanical properties, which make them interesting for fundamental studies and for applications in high-end electronics, spintronics, optoelectronics, energy harvesting, flexible electronics, DNA sequencing and personalized medicine. In this Review, the methods used to synthesize TMDCs are examined and their properties are discussed, with particular attention to their charge density wave, superconductive and topological phases. The use of TMCDs in nanoelectronic devices is also explored, along with strategies to improve charge carrier mobility, high frequency operation and the use of strain engineering to tailor their properties.

Two-dimensional transition metal dichalcogenides (TMDCs) are an emerging class of materials with properties that make them highly attractive for fundamental studies of novel physical phenomena and for applications ranging from nanoelectronics and nanophotonics to sensing and actuation at the nanoscale. The past years have seen a strong resurgence of interest in 2D TMDCs, sparked by the demonstration of the first transistor[1] and by the discovery of strong photoluminescence in MoS_2 monolayers[2,3].

TMDCs have a very long and fruitful history. Their structure was first determined by Linus Pauling in 1923 (REF. 4). By the late 1960s, around 60 TMDCs were known, at least 40 of them with a layered structure[5]. The first reports on the use of adhesive tapes for producing ultrathin MoS_2 layers, by Robert Frindt, date back to 1963 (REF. 6), and the production of monolayer MoS_2 suspensions was first achieved in 1986 (REF. 7). In parallel with the development of research on carbon nanotubes and fullerenes in the 1990s, Reshef Tenne and others led strong efforts in the area of inorganic fullerenes and nanotubes, which commenced with the discovery of WS_2 nanotubes and nested particles[8], followed by the synthesis of MoS_2 nanotubes and nanoparticles[9]. The rapid growth of graphene-related research that started in 2004 stimulated the development of techniques well-suited for working with layered materials, opening the way to new studies of TMDCs and, in particular, of their ultrathin films.

Several recent reviews cover the optical properties of TMDCs and their heterostructures, as well as their use in various photonics and optoelectronics applications[10–12]. In this Review, the focus is mainly on recent results related to the electronic properties of TMDCs. We start by introducing the structural phases and electronic band structure of TMDCs, examining in particular their charge density wave, superconducting and topological phases. We then examine the methods that can be used to synthesize these materials. The use of TMDCs in devices and the strategies that can be implemented to enhance mobility are discussed next, along with their high-frequency performance and the use of strain engineering to tune the materials properties.

Structure

TMDCs exist in several structural phases resulting from different coordination spheres of the transition metal atoms. The two common structural phases are characterized by either trigonal prismatic (2H) or octahedral (1T) coordination of metal atoms (FIG. 1a).

These structural phases can also be viewed in terms of different stacking orders of the three atomic planes (chalcogen–metal–chalcogen) forming the individual layers of these materials. The 2H phases correspond to an ABA stacking in which chalcogen atoms in different atomic planes occupy the same position A and are located on top of each other in the direction perpendicular to the layer. By contrast, the 1T phases are characterized by an ABC

[1] *Electrical Engineering Institute, École Polytechnique Fédérale de Lausanne (EPFL), CH-1015 Lausanne, Switzerland.*
[2] *Institute of Materials Science and Engineering, École Polytechnique Fédérale de Lausanne (EPFL), CH-1015 Lausanne, Switzerland.*
[3] *Institute of Physics, École Polytechnique Fédérale de Lausanne (EPFL), CH-1015 Lausanne, Switzerland.*

Correspondence to A.K.
andras.kis@epfl.ch

doi:10.1038/natrevmats.2017.33

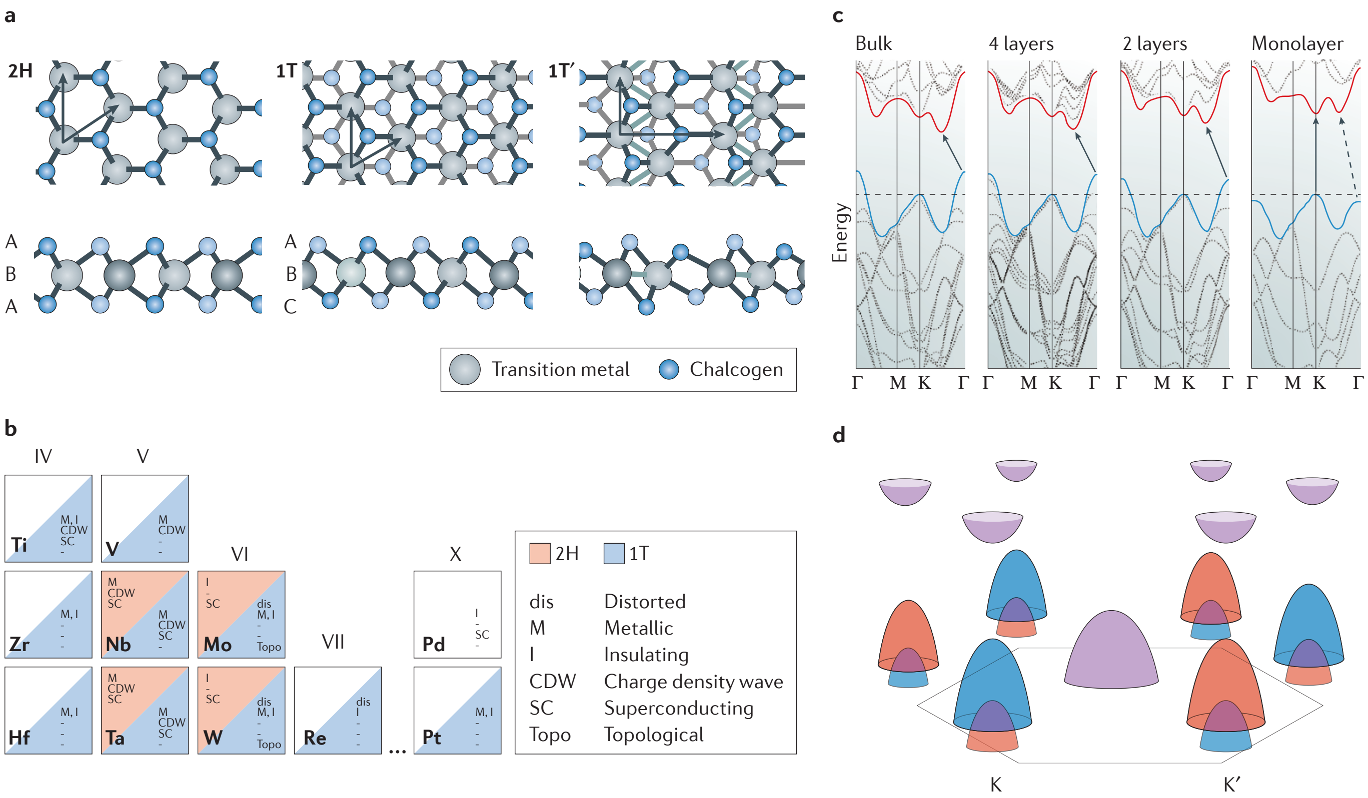

Figure 1 | **Structure and electronic properties of TMCDs. a** | Atomic structure of single layers of transition metal dichalcogenides (TMDCs) in their trigonal prismatic (2H), distorted octahedral (1T) and dimerized (1T′) phases. Lattice vectors and the stacking of atomic planes are indicated. **b** | 'Periodic table' of known layered TMDCs, organized based on the transition metal element involved, summarizing their existing structural phases (2H, 1T or other, as in the case of Pd-based TMDCs) and indicating the presence of distorted structural phases and observed electronic phases. **c** | Evolution of the band structure of 2H-MoS_2 calculated for samples of decreasing thickness. **d** | Schematic representation of the band structure of monolayer 2H-MoS_2, showing the spin splitting of the bands at the K and K′ points on the corners of the Brillouin zone. Orange and blue colours indicate up and down spin polarization. Panel **c** is adapted with permission from REF. 2, American Chemical Society. Panel **d** is adapted with permission from REF. 17, American Physical Society.

stacking order. Depending on the particular combination of transition metal (group IV, V, VI, VII, IX or X) and chalcogen (S, Se or Te) elements, the thermodynamically stable phase is either the 2H or 1T phase, but the other can often be obtained as a metastable phase. The current knowledge on the existence of the two phases, in either stable or metastable form, and on other properties of TMDCs is summarized in the 'periodic table' shown in FIG. 1b. For example, for five of six possible chemically distinct bulk TMDCs formed by group VI transition metals (metal = Mo or W; chalcogen = S, Se or Te) the 2H phase is thermodynamically stable and the 1T phase can be obtained as a metastable phase. An exception is represented by WTe_2, for which the stable bulk phase at room temperature is the orthorhombic $1T_d$ phase.

The structure of TMDCs is further defined by the stacking configuration of the individual layers in the case of multilayer and bulk samples, and by possible distortions that lower the periodicity. These distortions, if pronounced, can result in the formation of metal–metal bonds — as it happens, for example, in the dimerization of the 1T phase of group VI TMDCs, which results in the 1T′ phase, or in the tetramerization of rhenium dichalcogenides such as 1T-ReS_2 — or in weaker lattice distortions accompanying charge density wave phases, which display rich physics and complex phase diagrams, as discussed below.

Electronic band structure

The diversity of chemical compositions and structural phases of TMDCs results in a broad range of electronic properties, both from the point of view of the band structure character (metallic or insulating) and of the emergence of correlated and topological phases. We discuss here the basic features of the band structure of TMDCs formed by group VI transition metals Mo and W combined with S and Se (an overview of the electronic properties of TMDCs is presented in FIG. 1b). In their thermodynamically stable 2H phase, MoS_2, $MoSe_2$, WS_2 and WSe_2 are semiconductors. This property drew attention to these TMDCs as 2D materials for electronic devices[1]. The evolution of the band structure of 2H-MoS_2 as calculated from first principles[2] (density functional theory) upon reducing its thickness from bulk to monolayer is shown in FIG. 1c. The positions of the valence and conduction band edges change with decreasing thickness, and the indirect bandgap semiconductor bulk material turns into a direct bandgap semiconductor monolayer[2,3]. The calculated values for the bandgap of bulk and monolayer 2H-MoS_2 are 0.88 and 1.71 eV, respectively[13]. The experimental value for the bandgap of monolayer 2H-MoS_2 is 2.16 eV (REF. 13). Importantly, the valence band maximum and the conduction band minimum are located at the two inequivalent high-symmetry points K and K′, which correspond to the corners of the hexagonal Brillouin zone. This property is common to monolayer 2H-MoS_2 (and other group VI monolayer 2H-TMDCs) and to graphene, and enables the observation of valley-dependent physical phenomena and potential valleytronics applications.

Another important peculiarity of monolayer 2H-TMDCs is that they lack inversion symmetry, which results in a spin splitting of the electronic bands driven by the spin–orbit interaction. Because points K and K′ do not correspond to the time-reversal invariant momenta, the spin degeneracy of the conduction and valence band extrema at these points is lifted. This effect is particularly strong in the valence band, in which spin splitting values range from 0.15 eV in monolayer 2H-MoS_2 to 0.46 eV in 2H-WSe_2 (REF. 14). This trend is understood by considering that the spin–orbit interaction is a relativistic effect, and hence is stronger for heavier elements. Even though the spin splitting of the conduction band is about an order of magnitude weaker[15], it is not negligible. Because of time-reversal symmetry, the spin splitting of bands at K and K′ is opposite; the resulting band structure of monolayer 2H-MoS_2 relevant to realistic charge-carrier concentrations is schematically represented in FIG. 1d. This property is referred to as spin–valley coupling[16] and implies that the valley polarization of charge carriers is automatically translated into their spin polarization. This intrinsic property of TMDCs may be used to design spintronic devices that do not involve magnetic materials[17,18].

Charge density wave phases. At low temperature, a 1D metal with non-interacting electrons is unstable against a small periodic distortion of the underlying lattice, which is accompanied by the opening of a bandgap at the Fermi energy, resulting in insulating behaviour. The period of the distortion, which arises from the interaction between electrons and phonons, is given by $Q = 2k_F$, where k_F is the Fermi momentum[19,20]. Such a distortion leads to a modulation of the electronic charge density, the so-called charge density wave (CDW). Chan and Heine[21] demonstrated that a modulation of the charge density without a coupling to phonons cannot exist, therefore establishing the equivalence between CDWs and the concept of periodic lattice distortions. A 2D or 3D metal with a nested Fermi surface (that is, a Fermi surface with large parallel sections separated by a nesting vector Q_N) has a hidden 1D character and can also undergo a CDW distortion with periodicity Q_N at low temperature, owing to a logarithmic singularity in the electronic response function (or bare susceptibility)[19,21,22].

The discovery of CDW phases in the group V layered dichalcogenides, in both the 2H and 1T phases of TaS_2 and $TaSe_2$, and in 2H-$NbSe_2$, led to renewed interest in this theory[23,24]. The phenomenology of the CDW in dichalcogenides is rich and diverse and strongly depends on the chemical composition and crystalline phase of the material. For example, 2H-$NbSe_2$ undergoes a triple-Q transition at $T_{CDW} = 33$ K. This CDW is nearly commensurate (that is, the CDW wavelength is nearly an integer multiple of the lattice constant) and results in the formation of a superlattice with roughly 3 × 3 periodicity; the wave vectors are $Q_i = b_i/3(1 - \delta)$, where $\delta << 1$ represents the decommensuration, and b_i are the three reciprocal vectors of a triangular lattice[25]. Unlike in other CDW materials, the periodicity is almost independent of temperature and does not show any first-order transition to a commensurate phase, sometimes referred to as lock-in transition. The displacement of the atoms is very small (of the order of 0.05 Å) and the effect of the CWD on the physical properties is moderate, with only a small increase of the resistivity[26]. If the temperature is further lowered, the material becomes superconducting[27]. By contrast, 1T-TaS_2 exhibits a sequence of incommensurate ($T \approx 600$ K), nearly commensurate ($T \approx 350$ K) and commensurate ($T \approx 180$ K, with a $\sqrt{13} \times \sqrt{13}$ periodicity) transitions with a significant displacement of Ta atoms (up to 0.24 Å) that strongly effects the electronic properties (FIG. 2a). The transition from the normal state to the incommensurate phase is second order and is accompanied by a small jump in the resistivity. By contrast, the nearly commensurate and commensurate transitions are strongly first order and are associated with a large increase in resistivity[26,23]. Furthermore, the commensurate phase exhibits an interesting Mott insulating character arising from the narrowing of the conduction band induced by the distortion[28,29].

Following these results on bulk TMDCs, CDW phases in monolayer TMDCs were investigated, with particular attention to the CDW ordering vector and transition temperature[30]. First-principles calculations suggested that 2H-$NbSe_2$ in its monolayer form has a CDW phase with a different periodicity compared to that of the bulk (4 × 1, as opposed to 3 × 3 × 1) and a larger gain of electronic energy, hence a higher transition temperature[31]. Experimentally, a considerable enhancement of the transition temperature from $T_{CDW} = 33$ K in the bulk to $T_{CDW} = 145$ K in the monolayer was reported[32]. However, other authors have not found such an enhancement and reported a 3 × 3 periodicity for the monolayer[33]. By contrast, for the isostructural 2H-$TaSe_2$, first-principles calculations suggested the same periodicity for the bulk and the monolayer (3 × 3)[34]. Several studies addressed the CDW phase in thin films of 1T-TaS_2 with thicknesses down to one monolayer[35–37], but the evolution of the commensurate and nearly commensurate phases upon reducing the dimensionality is still under debate. Experimental studies of 1T-$TiSe_2$ with reduced thickness revealed a CDW with the same ordering vector as in the bulk (resulting in a 2 × 2 superlattice), with a slight enhancement of the critical temperature[38,39]. The absence of a hole pocket in the Fermi surface at the Γ point indicates that the pristine material is a small bandgap semiconductor rather than a semimetal with a small

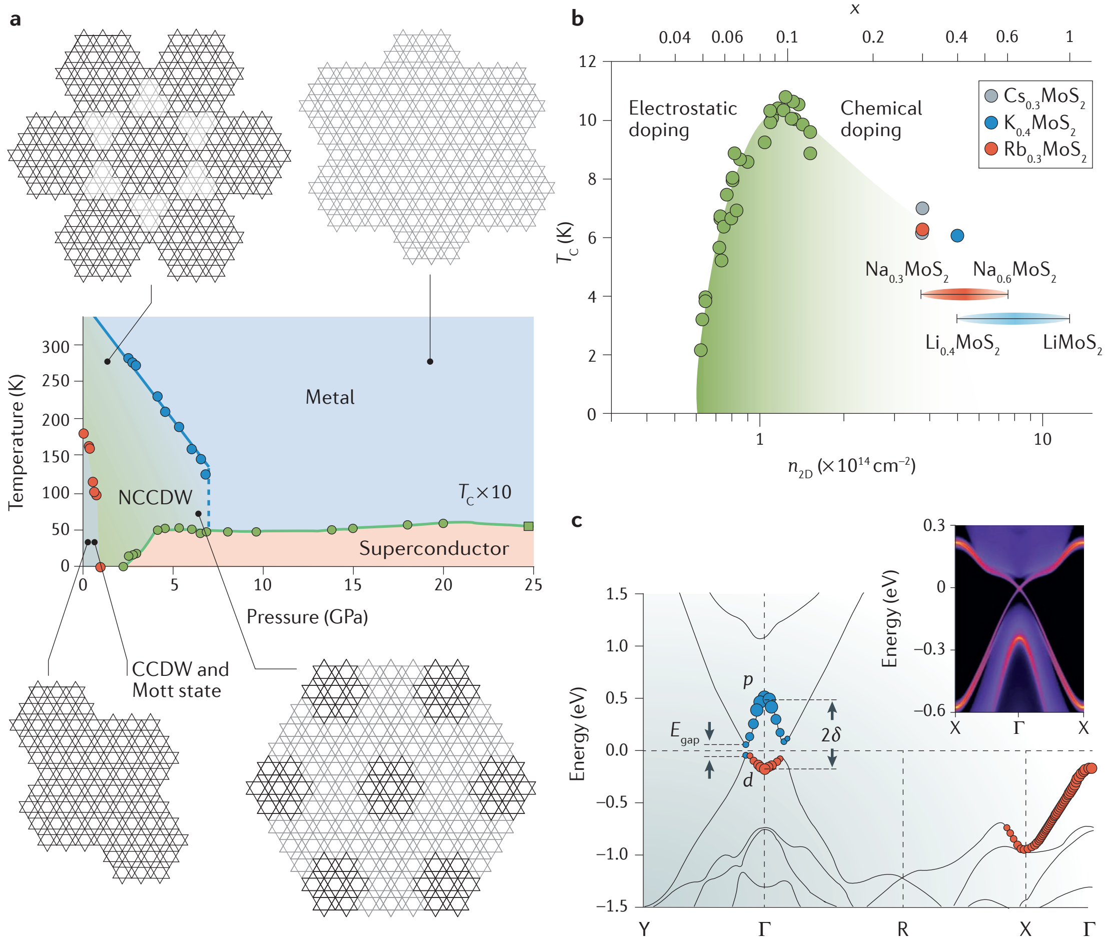

Figure 2 | **Correlated and topological phases of TMDCs. a** | Temperature–pressure phase diagram of 1T-TaS$_2$ showing various charge density wave (CDW) phases. The deformation patterns corresponding to the different phases are shown. **b** | Phase diagram of superconductivity in electrostatically and chemically doped 2H-MoS$_2$. **c** | Band structure of monolayer 1T′-MoS$_2$ showing the band inversion characteristic of the quantum spin Hall phase. The inset shows the dispersion of the topological edge states. 2δ, inverted gap energy; CCDW, commensurate CDW; E_{gap}, fundamental gap energy; n_{2D}, electron carrier density; NCCDW, nearly commensurate CDW; T_C, superconductive transition temperature. Panel **a** is adapted with permission from REF. 29, Macmillan Publishers Limited. Panel **b** is adapted with permission from REF. 56, AAAS. Panel **c** is adapted with permission from REF. 62, AAAS.

band overlap (this question has long been debated for bulk samples, with several experiments supporting either view). The CDW in 1T-TiSe$_2$ is therefore a semiconductor-to-semiconductor transition, with a slight increase of the bandgap induced by the distortion. The electronic structure of 1T-TiSe$_2$ is strongly reminiscent of the excitonic insulator proposed by Kohn, Jérome and Rice[40,41], but never unambiguously observed in real systems. The question of whether the CDW in TiSe$_2$ should be regarded as a manifestation of an exciton condensate, or simply as driven by electron–phonon interactions, is still a matter of debate[38,39].

Although the theory underlying CDW driven by Fermi surface nesting is well established, the question of whether this theory actually applies to TMDCs (or any real system) is debated. The difficulty of identifying a nesting vector by inspecting the Fermi surface and the strong modifications of the electronic structure induced by the distortions have led some to argue that the Fermi surface nesting hardly has a role in TMCDs, and that the distortions are mainly due to strongly anisotropic electron–phonon matrix elements with enhanced values at the CDW wave vector[30–34].

Superconductivity. Interestingly, all bulk TMDCs displaying a CDW state in their phase diagram also exhibit superconductivity, with the exception of 2H-NbS$_2$, which is only superconducting[42]. The two phases can either compete or coexist. However, superconductivity is much more robust than the CDW phase, as it does not depend on the nesting of the Fermi surface. In TMDCs, the superconducting state can be either intrinsic or induced by chemical doping, electrostatic doping or applied pressure. In the 2H phase of NbSe$_2$, TaS$_2$ and TaSe$_2$, superconductivity coexists with the CDW phase at low temperatures[27,43–45]. In TMDCs with the 1T phase, such as semimetallic 1T-TiSe$_2$ (REFS 46,47) and 1T-TaS$_2$ (REFS 29,48), the superconducting state emerges as the CDW order melts, either under applied pressure or upon chemical doping by means of copper intercalation. A competition between a low-temperature distorted phase and a superconducting phase was also observed in the newly found material $IrTe_2$. The exact nature of the distorted phase has not been clearly identified yet; its suppression upon chemical doping leads to superconductivity with a critical temperature of up to 3 K (REF. 49).

The superconducting behaviour of bulk TMDCs persists in the 2D limit. Recently, the first experimental evidence for truly 2D intrinsic superconductivity in TMDCs was reported for monolayer 2H-$NbSe_2$ (REF. 33). The 2D superconducting state is of the Kosterlitz–Thouless type[50], as evidenced by the voltage–current characteristic measured close to the critical temperature[51,52]. Although the critical temperature ($T_C = 3K$) is even lower than that of the bulk material ($T_C = 7\,K$), the in-plane critical field B_{C2} (the minimum magnetic field required to destroy the superconducting state) is an order of magnitude larger than that of the bulk and, more importantly, about seven times larger than the paramagnetic Pauli limit[51]. The enhancement of the in-plane critical field is not a new phenomenon in itself, but the underlying mechanism is unusual and is understood as arising from the combination of reduced dimensionality and strong spin–orbit coupling[53]. In a monolayer 2H phase TMDC, the spin splitting of the K and K′ valleys can be seen as an effective out-of-plane Zeeman field. Because of the spin–valley coupling, such spin splitting is compatible with Cooper pairing, and therefore the superconducting state in monolayer TMDCs is characterized by an Ising-like polarization of spins in the out-of-plane direction. This makes the superconducting state more robust against in-plane magnetic fields. In addition to the theoretical interest, it was pointed out that Ising superconductors could be useful for observing topological superconductivity and as an alternative route to engineer Majorana fermions in solid-state systems[53–55].

Superconductivity can also be induced in gated thin films of 2H-MoS_2 (FIG. 2b), in which electrostatic charge doping accumulates charge carriers in the outer layer, simulating a monolayer doped sample[52,56,57]. Superconductivity induced by gating has also been realized in thin films of 2H-WS_2 and 2H-$MoSe_2$ (REFS 58,59).

Topological phases. TMDCs have also attracted considerable interest as materials that could host novel topological electronic phases[60,61]. According to theoretical predictions, monolayer group VI TMDCs in their 1T′ phase exhibit a band structure with inverted chalcogen p and transition metal d bands[62] (FIG. 2c). In addition, the presence of a relatively strong spin–orbit interaction results in the opening of bandgaps of a few tens of millielectronvolts in 1T′ sulfides and selenides of molybdenum and tungsten. This gives rise to the quantum spin Hall phase, or, equivalently, to the 2D Z_2 topologically insulating phase, characterized by the presence of helical edge states immune to backscattering. These theoretical predictions are still awaiting experimental confirmation, but TMDC-based quantum spin Hall insulators would enable technological applications of this topological electronic phase. These 2D materials are certainly more suitable for practical applications than other quantum spin Hall insulators known to date: that is, HgTe/CdTe[63,64] and InAs/GaSb[65] quantum wells and bilayer Bi[49,66,67]. Bulk distorted 1T-phase tellurides of molybdenum and tungsten are semimetals, which gives rise to very large non-saturating magnetoresistance in WTe_2 (REFS 68,69). The non-centrosymmetric polymorphs of these materials were predicted to host a Weyl semimetal phase[70–72], which was, to some degree, experimentally confirmed[73,74].

Synthesis

MoS_2 and WS_2 are probably the only TMDCs that occur in nature in the form a layered crystal. The first high-performance transistors made of monolayers of MoS_2 were obtained from crystals of the naturally occurring mineral molybdenite[1]. Bulk crystals of other TMDCs are grown using the chemical vapour transport method[5], which enabled the first studies of the optical and electrical properties of MoS_2, $MoSe_2$ and WSe_2 crystals in the 1960s[5]. In this growth method, the precursors (Mo and Se in the case of $MoSe_2$)[75] are mixed in stoichiometric proportions with the addition of a transport agent (I_2, Br_2 or ICl_3) and put into an evacuated ampoule inside a multi-zone furnace with a varying temperature gradient. The material is transported to the colder part of the ampoule, where crystal growth takes place. A detailed review of crystal growth and characterization can be found in REF. 76.

High-quality natural or synthetic crystals can be used as a source of thin flakes. Similarly to graphene, which can be obtained by mechanical peel-off with sticky tape from graphite, single crystals of TMDCs can serve as a source of monolayers[1,77,78], which can then provide a platform for a range of fundamental studies and device demonstrations. Because micromechanical exfoliation requires only bulk crystals, a decent optical microscope and adhesive tape, it is a very popular method for rapid prototyping of devices based on TMDCs and other layered materials, and has greatly contributed to the rapid expansion of research in this area. However, this method is not scalable; moreover, the relatively small areas of uniform material and the haphazard nature of material deposition can be limiting factors for more extensive studies. Liquid-phase exfoliation based on organic solvents[79,80] is a scalable alternative to mechanical exfoliation and allows the production of solutions containing flakes with controllable thickness. The first experiments on liquid-phase exfoliation through Li intercalation date back to the 1970s[81], with a report on solutions containing single-layer MoS_2 from the 1980s[7]. Recent methods for the exfoliation of TMDCs in liquid using Li intercalation are being intensively explored[82,83]. The drawbacks of exfoliation through Li intercalation include reported phase transitions from the semiconducting 2H to the metallic 1T phase[82,84,85] and the limited size of the flakes, which results in overlaps between the flakes and in a large in-plane resistance of the films[82].

One of the first scalable methods developed for the direct growth of TMDCs was molecular beam epitaxy (MBE). The principle of operation is schematically illustrated in FIG. 3a through the example of the growth of GaSe on MoS_2. Detailed information on this growth method can be found in REF. 86. An ultrahigh vacuum chamber (with pressure typically below 10^{-10} mbar) contains several sources — in this case Ga and Se — to form molecular beams. Deposition is performed on a preheated substrate while the thickness and substrate crystallinity are monitored *in situ* by reflection high-energy electron diffraction and low-energy electron diffraction. The group of Atsushi Koma published numerous reports on the MBE growth of TMDCs in the 1980s and 1990s, demonstrating the successful growth of $MoSe_2$ and GaSe on a number of substrates, including other layered materials[87–90]. MBE-based growth of 2D materials largely differs from traditional 3D epitaxy. Because TMDCs do not contain dangling bonds, they can in principle be grown on other layered materials and passivated surfaces (for example H-passivated Si) without the need to satisfy lattice matching conditions. The weak van der Waals interaction can be exploited to achieve epitaxial growth, in which the lattice structure of the substrate can be used to align the orientation of the overlayer[91] — an essential requirement for growing high-quality films. Epitaxial growth can occur either if the substrate and the overlayer are lattice-matched, such as for $MoSe_2$ on GaAs, or if a commensuration condition can be satisfied, such as for MoS_2 on sapphire[91]. If these conditions are not met, the resulting films will be polycrystalline and contain many dislocations, such as for MBE-grown $MoSe_2$ on an amorphous SiO_2 substrate[92]. Such defects and grain boundaries can result in variable-range hopping through localized states in MBE-grown $MoSe_2$ and $MoTe_2$ on sapphire substrates[93]. MBE performed in ultrahigh vacuum growth chambers combined with scanning tunnelling microscopy or angle-resolved photoelectron spectroscopy provided access to the intrinsic properties of materials such as $MoSe_2$ (REFS 94,95) and $NbSe_2$ (REF. 33). Furthermore, various types of vertical heterostructures of 2D materials could be realized, for example, $SnSe_2/WSe_2$ (REF. 96), $MoSe_2/Bi_2Se_3$ (REF. 97) and $MoSe_2$/graphite[98]. Thus, MBE is a useful tool for fundamental studies of 2D materials and their combinations, although the electrical properties of as-grown films require further improvement.

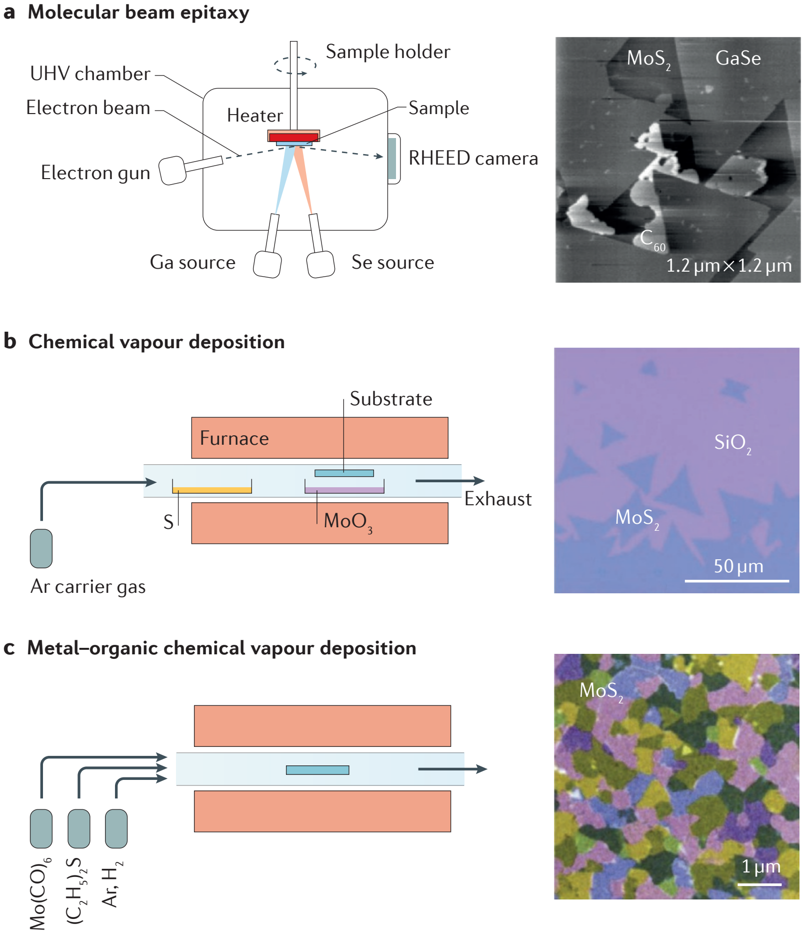

Figure 3 | **Growth methods for the synthesis of ultrathin TMDCs. a** | In molecular beam epitaxy, high-purity elemental source materials are co-evaporated in ultrahigh vacuum. The right panel is an atomic force microscope image of monolayer GaSe grown on MoS_2. **b** | Chemical vapour deposition is based on the direct chemical reaction between different precursor materials. An optical image of triangular single-crystalline domains of MoS_2 grown on SiO_2 is shown on the right. **c** | Metal–organic chemical vapour deposition is based on the decomposition of metal–organic precursors and their subsequent chemical reaction. On the right, a false-colour dark-field transmission electron microscopy image shows a continuous monolayer of MoS_2 with different grain orientations. RHEED, reflection high-energy electron diffraction; TMDC, transition metal dichalcogenide. Panel **a** is adapted with permission from REF. 90, Elsevier. Panel **b** is adapted with permission from REF. 220, American Chemical Society. Panel **c** is adapted with permission from REF. 110, Macmillan Publishers Limited.

The most practical method for the synthesis of high-quality TMDCs is chemical vapour deposition (CVD, FIG. 3b). This method does not require ultrahigh vacuum chambers and is thus cheap and relatively easy to integrate into existing industrial processes. The first reports of MoS_2 synthesis were based on the sulfurization of Mo pre-deposited on the substrate[99], upon dip coating of substrates in a $(NH_4)_2MoS_4$ solution followed by annealing in gas flow[100,101], or upon the growth of multilayers from MoO_3 and S precursors[102]. However, in these early reports there was no control over the material thickness; only in 2013 the growth of monolayer domains of MoS_2 on SiO_2 was reported in two simultaneous publications[103,104]. The working principle of CVD is shown in FIG. 3b; in the example shown, MoO_3 and S react at elevated temperature, leading to the growth of MoS_2 on the substrate. The as-grown domains on SiO_2 have good optical and electrical properties, displaying room temperature field-effect mobilities on the order of $5\,cm^2\,V^{-1}\,s^{-1}$ (REFS 103,104), but have random lattice orientation with respect to each other and thus form grain boundaries of different types. These grain boundaries are predicted to have a plethora of electronic properties, for example, 60° grain boundaries could have metallic nature[105]. The investigation of the electrical transport properties of large-area devices fabricated from similar materials showed that the presence of grain boundaries decreases the mobility of large area films[106]. The need to control the orientation of domains motivated further developments; for example, atomically smooth c-plane sapphire was used to promote the epitaxial CVD growth of monolayer MoS_2 (REF. 91). In contrast to the growth on SiO_2 substrates, systematic alignment was observed, owing to the commensurate lattices of MoS_2 and sapphire. A two-probe field-effect mobility of ~25 $cm^2 V^{-1} s^{-1}$ was preserved on a length scale of 80 μm, through ~16 grain boundaries. Thus, the engineering of the alignment of separate flakes can lead to a better control of the electrical properties of large area films.

A growth method related to CVD is metal–organic CVD (MOCVD), which is based on the use of gas-phase precursors[107–110], and was first used for TMDC synthesis in the 1990s[107]. Gas precursors are supplied to the main chamber with controlled flux (FIG. 3c). Recently, wafer-scale synthesis of MoS_2 and WS_2 on various substrates was demonstrated, and the resulting samples displayed good electrical properties. For example, the MoS_2 sample had an electron mobility of ~30 $cm^2 V^{-1} s^{-1}$ (REF. 110). The discussed CVD results mainly regard MoS_2 growth. In addition to MoS_2, other TMDCs, such as $MoSe_2$ (REFS 111–113), WS_2 (REFS 107,110,114–120), WSe_2 (REFS 109,121–123), ReS_2 (REFS 124–126), $ReSe_2$ (REF. 127), $MoTe_2$ (REFS 128,129) or WTe_2 (REF. 129), can be grown both by CVD and MOCVD. However, the electrical properties of the large-area films of these materials are not yet well characterized and require further investigation.

Different types of TMDC heterostructures can also be grown using CVD. In particular, atomically sharp interfaces between monolayers of MoS_2 and $MoSe_2$ (REF. 130), WSe_2 and $MoSe_2$ (REF. 131), MoS_2 and WS_2 (REF. 132), $MoSe_2$ and WSe_2 (REF. 131), WS_2 and WSe_2 (REF. 130), and WSe_2 and MoS_2 (REF. 133) have been realized by CVD. The benefits of this approach over manual assembly through transfer techniques are that the interfaces are atomically sharp, as shown in FIG. 4a,b, and that there are no residues from the transfer process. Theoretical modelling predicts exotic behaviours for such heterostructures[134]: for example, efficient charge separation[134] and valley filtering within one material[17]. Moreover, these artificial materials could be used as p–n diodes without resorting to *in situ* doping or transfer processes, as shown in the example in FIG. 4c, where a lateral boundary between WSe_2 and MoS_2 serves as a p–n junction[134] and can be used as a light-emitting diode.

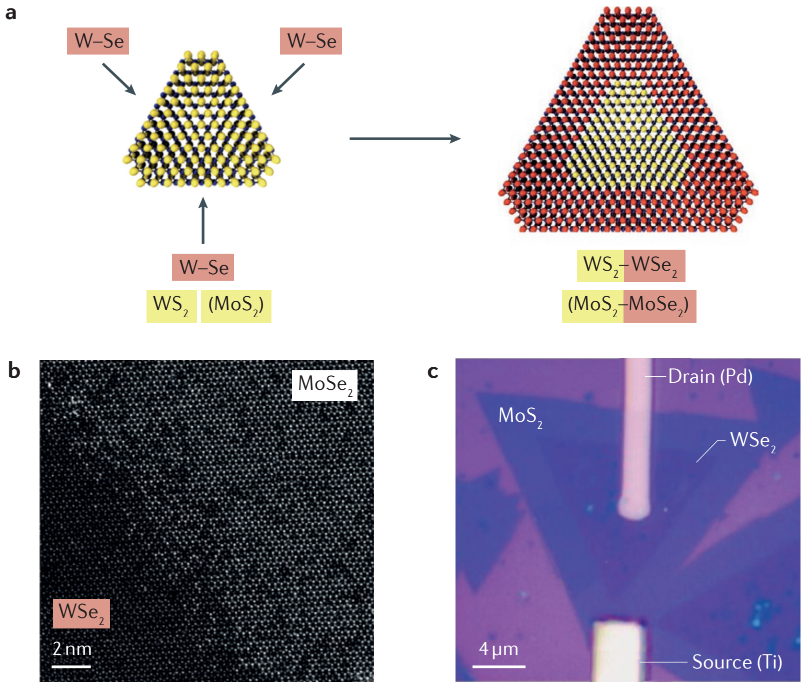

Figure 4 | **Examples of synthesis of 2D TMDC lateral heterostructures.** **a** | Schematic drawing showing the growth of lateral heterostructures based on 2D transition metal dichalcogenide (TMDC) materials. **b** | High-angle annular dark-field scanning transmission electron microscopy image of the lateral heterostructure formed between $MoSe_2$ and WSe_2. **c** | Optical image of a p–n junction based on a MoS_2/WSe_2 lateral heterostructure. Panel **a** is adapted with permission from REF. 130, Macmillan Publishers Limited. Panel **b** is adapted with permission from REF. 131, Macmillan Publishers Limited. Panel **c** is adapted with permission from REF. 133, AAAS.

Semiconductor devices

Mobility engineering. The suitability of 2D materials for applications based on quantum transport is determined by the mean free path of charge, spin or valley carriers, which for charge carriers is directly proportional to the charge carrier mobility. Although the theoretically predicted values for the charge carrier mobility are very promising for 2D TMDCs[135–137], the mobility is in practice limited by disorder and by the presence of scattering sources. These can be intrinsic charged point defects or defects in the surrounding dielectric or at the semiconductor/dielectric interface, which can trap charges and scatter mobile charge carriers. Intrinsic and remote optical phonons in the environment of the 2D semiconductor can further limit the mobility close to room temperature.

Theoretical calculations for monolayer MoS_2 predict a room-temperature electron mobility in the range of 10–1,000 $cm^2 V^{-1} s^{-1}$ and low-temperature values exceeding 10^5 $cm^2 V^{-1} s^{-1}$, depending on factors such as the impurity density and the dielectric environment[135,138,139]. The measured mobility for atomically thin MoS_2 is almost two orders of magnitude lower than that of its bulk counterpart[1,78,140]. The degradation of the mobility when going from bulk to thin-film samples can be understood considering that atomically thin materials are more sensitive to environmental factors owing to their increased surface-to-volume ratio. Remote optical phonons and Coulomb scattering from the interfacial charge traps are proposed to be the dominant reasons behind the low carrier mobility in MoS_2 atomically thin layers.

The encapsulation of monolayer MoS_2 with a HfO_2 dielectric layer enabled the first demonstration of a transistor based on monolayer MoS_2 (REF. 1) and, in general, on a 2D TMDC semiconductor. Subsequent temperature-dependent mobility measurements[141] on monolayer MoS_2 in a multiprobe geometry gave the first insights into mobility degradation in monolayer TMDCs. For devices with an exposed MoS_2 channel, mobility increases with increasing temperature until it reaches a peak value at $T \approx 200$ K, after which it starts to degrade again, indicating that scattering from charged impurities is the dominant mechanism limiting the mobility at low temperatures. In this regime, increasing the temperature increases the thermal energy of the carriers and their thermal velocity, which in turn reduces the scattering cross section. Above ~200 K, phonon scattering becomes the dominant scattering mechanism. As temperature increases, the number of phonon modes available for scattering increases, resulting in reduced mobility. The deposition of a thin layer of a dielectric material with a high dielectric constant κ, such as HfO_2, on MoS_2 enhances the low-temperature mobility, owing to the effective screening of the static Coulomb scattering from charged impurities[139] (FIG. 5a). Adding a metallic top gate on the surface of the dielectric results in a further increase in the mobility; the measured electron mobility has an impurity-limited value of 120 – 180 $cm^2 V^{-1} s^{-1}$. The mobility starts decreasing above 20 K (FIG. 5a) and in the 100 – 300 K range it can be fitted using the power-law dependence $\mu \approx T^{-\gamma}$, where γ has values in the range of 0.55 – 0.78. This value is much smaller than the experimental values found for bulk crystals ($\gamma = 2.6$ (REF. 140)) or for bare monolayers ($\gamma = 1.4$ (REF. 141)), showing that the presence of the top gate can reduce the rate of mobility degradation with rising temperature, and can allow the observation of the metal–insulator transition and of band transport[141]. Temperature-dependent conductivity measurements further support this interpretation. Bare MoS_2 devices show transport features that can be fitted using a variable-range hopping model, which is typical of electrical transport through localized states in disordered low-dimensional systems. Here, the disorder can come from intrinsic defects, adsorbates or defects in the substrate. In the presence of a material with a high dielectric constant and top gate, the transport displays thermally activated behaviour with conductance proportional to e^{-E_a/k_BT} (where E_a is the activation energy and k_B is the Boltzmann constant), which indicates the effective screening of charged impurities and results in a reduction of disorder.

Dielectric environment engineering promises an effective approach to mobility enhancement[139,141]. However, it is important to understand the intrinsic electrical transport properties of 2D semiconductors in the absence of the dielectric layer, which can influence the charge impurity scattering or the remote optical phonon scattering. A promising avenue for the achievement of high mobilities consists in the elimination of external impurities, such as adsorbates from the atmosphere or impurities originating from the fabrication process. This can be done by *in situ* annealing in vacuum[142], which enhances the conductivity of the MoS_2 channel, increases n-type doping levels and significantly reduces the contact resistance, resulting in low-temperature mobilities of 250 $cm^2 V^{-1} s^{-1}$ and 375 $cm^2 V^{-1} s^{-1}$ in unencapsulated mono- and bilayer MoS_2, respectively. Combining this approach with the use of substrates with a high dielectric constant results in the highest room-temperature mobility reported to date (~150 $cm^2 V^{-1} s^{-1}$ for monolayer MoS_2 deposited on HfO_2)[143]. Using polymer substrates with high optical phonon frequencies also resulted in improved mobility for $MoSe_2$ (REF. 144).

The encapsulation of MoS_2 in hexagonal boron nitride[145] (hBN; FIG. 5b), combined with the use of graphene as the contact between the metal and the MoS_2 layer[146], resulted in the highest low-temperature mobilities measured to date, owing to the reduced number of adsorbates and the low roughness of the hBN substrate. Magnetotransport measurements revealed low-temperature values of the Hall mobility reaching 34,000 $cm^2 V^{-1} s^{-1}$ for six layers of MoS_2 and 1,000 $cm^2 V^{-1} s^{-1}$ for monolayer MoS_2 (FIG. 5c). The values for the critical exponent γ are in the range of 1.9–2.5, which is higher than that for HfO_2 (REF. 141). This could be attributed to the less efficient suppression of homopolar phonon modes by a relatively thin hBN film as compared to 30 nm of HfO_2 with metallic gates. Modelling of the various potential scattering sources suggests that long- and short-range interfacial scattering are the limiting factors for the low-temperature impurity-dominated mobility[145]. Because the impurity-dominated mobility increases with the layer thickness, it can be excluded that short-range intrinsic defects and bulk charged impurities have a role in determining its value. A similar improvement in the mobility as a result of encapsulation was reported for WS_2 (REFS 147–149).

These high mobility values enabled the observation of Shubnikov–de Haas (SdH) oscillations in the electrical conductivity at low temperatures and high magnetic fields. However, for the MoS_2 sample with graphene contacts encapsulated in hBN[145], the presence of high-mobility graphene implies that the SdH oscillations could contain contributions both from graphene and MoS_2. The contribution of graphene to the SdH oscillations is suggested by the observation of plateau-like behaviour in the measured Hall resistance, which could be attributed to the onset of the quantum Hall states in graphene and by the discrepancy between the carrier densities estimated from Hall measurements and from SdH oscillations. Magnetoresistance measurements performed on p-type WSe_2 encapsulated in hBN[150] with metallic electrodes enabled the observation of SdH oscillations (FIG. 5d) and of the quantum Hall states in mono- and bilayer WSe_2. In this case, the absence of graphene excludes any contribution to the SdH oscillations other than that from the WSe_2 layers, and the carrier density extracted from the SdH oscillation frequencies agrees well with the Hall measurements assuming a twofold degeneracy of the Landau levels.

The reduction of extrinsic sources of scattering highly improves the low-temperature mobility. An avenue for further improvement would consist of implementing the strategies used for controlling the intrinsic limiting factors for the mobility, such as crystal defects. By combining methods that reduce intrinsic scattering with encapsulation techniques, which reduce extrinsic scattering, could lead to further improvements in both room- and low-temperature mobilities.

High-frequency operation. High mobilities are important for device operation based on quantum transport. However, reducing the channel length can result in improved transistor performance and operating frequency, reducing the importance of the mobility for devices with sub-10 nm gate lengths. At such short length scales many 2D materials are expected to show ballistic transport. The main limiting factor for device performance in this case is direct tunnelling between the contacts, which can degrade the off-state currents and thus lower the on/off current ratio.

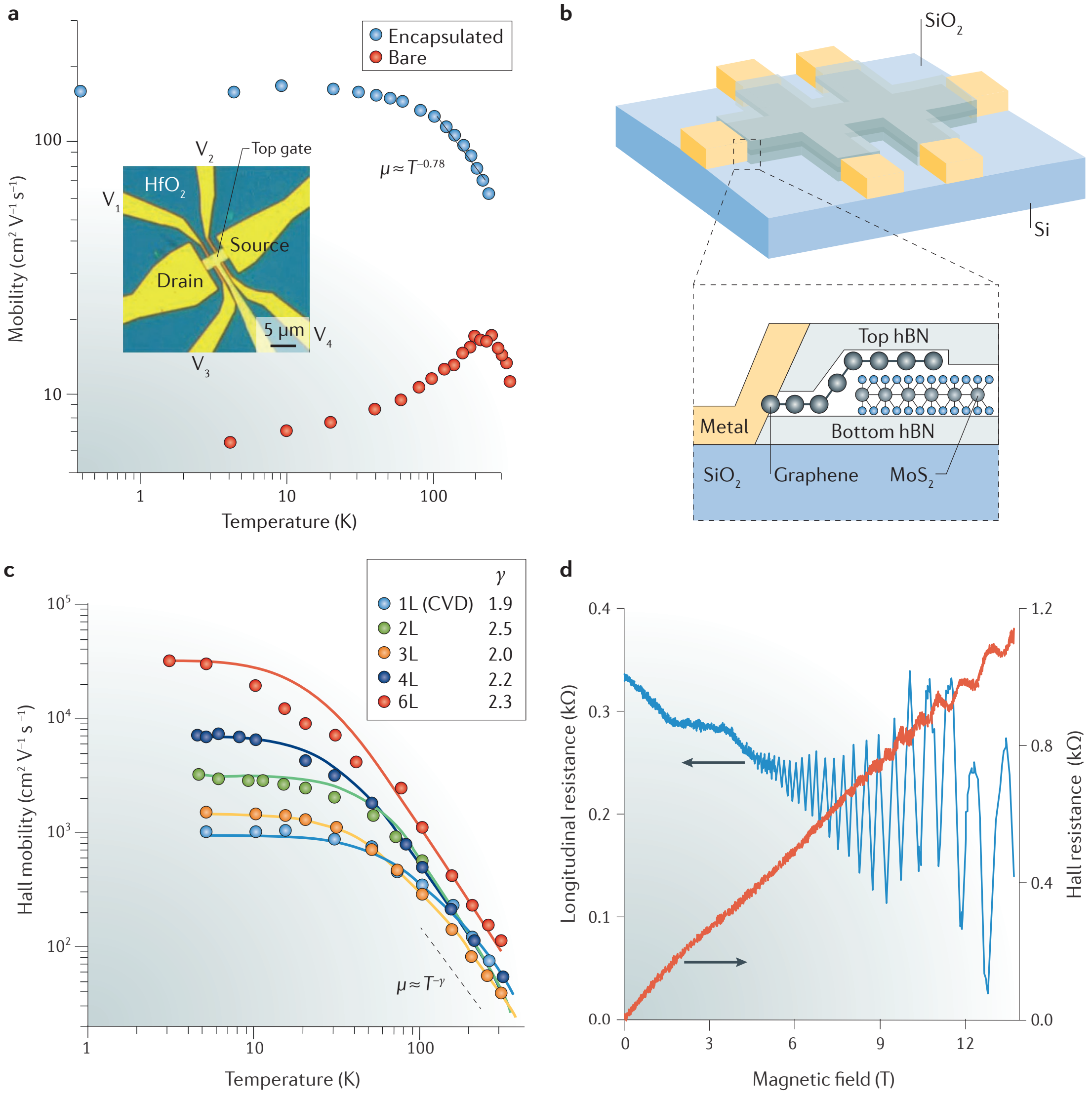

Figure 5 | **Mobility in TMDC-based devices. a** | Temperature dependence of the mobility for a transistor based on monolayer MoS_2 with the exposed channel, and for the same transistor encapsulated in HfO_2 and with a top gate. This last device is shown in the inset. **b** | Schematic depiction of a MoS_2 Hall bar device encapsulated in hexagonal boron nitride (hBN). The close-up view shows a cross section of the metal–graphene–MoS_2 contacts. **c** | Temperature dependence of the Hall mobility, μ_h, for MoS_2 devices with various thicknesses encapsulated in hBN. The dashed line shows the power law $\mu_h \approx T^{-\gamma}$; the values of γ used for the fit for each device are shown. The low-temperature values of μ_h reach 34,000 $cm^2 V^{-1} s^{-1}$ for 6 layers of MoS_2 and 1,020 $cm^2 V^{-1} s^{-1}$ for monolayer MoS_2. **d** | Shubnikov–de Haas oscillations in encapsulated monolayer WSe_2. The longitudinal (R_{xx}) and Hall (R_{xy}) resistances are measured as a function of the magnetic field at a temperature of 1.6 K and a hole density of 7.9×10^{12} cm^{-2}. Shubnikov–de Haas oscillations appear in R_{xx} starting at magnetic field ~4.5 T. The oscillations exhibit a density-to-frequency ratio of $2e/h$ (where e is the charge of the electron and h is the Planck constant), which is an indicator of twofold degenerate Landau levels. The Shubnikov–de Haas oscillations in R_{xx} are followed by the appearance of steps in R_{xy}, indicating the developing quantum Hall states. CVD, chemical vapour deposition; L, layer; n_{2D}, 2D carrier density; TMDC, transition metal dichalcogenide. Panel **a** is adapted with permission from REF. 141, Macmillan Publishers Limited. Panels **b** and **c** are adapted with permission from REF. 145, Macmillan Publishers Limited. Panel **d** is adapted with permission from REF. 150, American Physical Society.

For devices based on graphene, owing to the high mobility and saturation velocity, the high-frequency performance exhibits low impedance, large transconductance ($g_m = dI_{ds}/dV_{gate}$) and high intrinsic cut-off frequency f_T (the frequency at which the current gain becomes unity). However, in addition to the current gain, which is relevant in demodulators for telecommunication, the power and voltage gain are important factors for high-frequency operation. For graphene, because of the absence of a bandgap, the maximum oscillation frequency f_{max} (the power gain cut-off frequency) is not as high as f_T. Also, the voltage gain ($A_v = g_m/g_{ds}$) is limited by the relatively high drain conductance g_{ds}, because the absence of a bandgap makes it difficult to achieve current saturation in graphene transistors[151,152].

High-frequency 2D TMDC devices, owing to the presence of a sizable bandgap, are expected to exhibit voltage and power gain in addition to the current gain. Simulations of ballistic quantum transport predict that values of f_T above 100 GHz could be obtained in MoS_2 transistors with a channel length of 15 nm (REF. 153). Although still far from this number, the first radio-frequency MoS_2 devices[154] integrated with coplanar waveguides showed operation in the gigahertz frequency range with a de-embedded cut-off frequency for current amplification (f_T) of 6 GHz, as well as a power gain cut-off (f_{max}) of 8.2 GHz and voltage amplification above 5 GHz, demonstrating the feasibility of realizing logic circuits based on TMDCs operating in the gigahertz range.

Reducing the channel length below 100 nm and improving the contacts by edge injection[155] results in $f_T = 25$ GHz, $f_{max} = 16$ GHz and voltage amplification up to 45 GHz. Further optimization of the contacts and device geometry could be achieved using self-aligned devices[156]. In addition, the promising radio-frequency behaviour of MoS_2 transistors enables the fabrication of electronic elements such as radio frequency amplifiers and digital inverters on rigid and flexible substrates[156,157]. Although the reported radio-frequency performance of flexible MoS_2 transistors ($f_T \approx 13.5$ GHz, $f_{max} \approx 10.5$ GHz) is comparable to that of flexible devices based on silicon nanomembranes ($f_T \approx 3.8$ GHz, $f_{max} \approx 12$ GHz)[158] and worse than that of flexible devices based on III–V semiconductors ($f_T \approx 105$ GHz, $f_{max} \approx 22.9$ GHz)[159], the realization of radio-frequency electronics on flexible substrates exploits the extraordinary mechanical properties of 2D materials, such as the high Young's modulus, high breaking strength and elastic behaviour. These properties make TMDCs an attractive alternative to commercial semiconductors for state-of-the-art flexible radio-frequency circuits. More detailed studies are needed to investigate the radio-frequency performance of flexible MoS_2 devices subject to deformation.

Strain engineering in TMDCs. The high strength of 2D TMDCs, which can endure strains of up to 10% before breaking[160], makes them promising candidates for strain engineering, because it allows the application of strains high enough to induce considerable changes in the materials properties. Their three-fold symmetry is also advantageous, making it possible to vary the properties using lower strains as compared with those needed in graphene, which has six-fold symmetry[161,162]. Calculations suggest that tensile strain would reduce the bandgap of semiconducting TMDCs[163–165], turning them into indirect semiconductors[163,164,166–172], and that the bandgap would fully close at a level of biaxial tensile strain of ~10%[163,164]. In addition to the bandgap, strain is expected to modulate the charge carrier effective masses[166,173], thermal conductivity[174,175], dielectric properties[173], spin–orbit coupling[176–178] and on-state currents in TMDC transistors[168,179,180]. Thus, strain engineering is a viable approach for the realization of various types of electronic, optoelectronic, electromechanical and spintronic devices with tunable characteristics[181].

Heterostructures formed by vertically stacking different TMDCs are also expected to be strongly affected by strain[182,183], which could originate from the interlayer interactions and from lattice mismatch. As in the case of monolayers, strain could be used to modulate the bandgap of hybrid bilayers[183] and multilayers. Other theoretical studies investigated the effect of strain on anisotropic TMDCs[184], of which $ReSe_2$ and ReS_2 are the best known examples. Their distorted 1T phase structure gives rise to a strong dependence of the strain response on the direction in which the strain is applied. The carrier mobility might be significantly enhanced if strain is applied in the direction perpendicular to the layers.

A wide range of strategies was exploited for applying strain in nanomechanical devices incorporating 2D TMDCs. These include the use of: wet-etching[185] (FIG. 6a) or polymer sacrificial layers[186] for the fabrication of suspended devices; transfer on a substrate with pre-patterned holes or trenches[187]; tailored nanopatterns[188]; flexible[189–191] or pre-stretched[192] substrates (FIG. 6b); and thermal[193] or piezoelectric expansion[194]. Optical techniques, such as photoluminescence spectroscopy[188–191,194,195], Raman spectroscopy[189,191,194,196] and absorption spectroscopy[190], have been used to monitor the effect of strain on the optical bandgap and vibrational modes of 2D MoS_2 and other TMDCs[197,198]. Photoluminescence measurements[190] confirmed theoretical predictions that strain could reduce the bandgap[163] and revealed a redshift of ~70 meV/% strain for the direct gap transition and of ~110 meV/% strain for the indirect gap transition in bilayer MoS_2. However, photoluminescence spectroscopy can only be used on mono- and bilayer samples. Raman spectroscopy showed that the strain-induced symmetry breaking shifts the Raman modes in mono- and bilayer MoS_2, splitting the doubly degenerate in-plane vibrational modes[189].

Spatially inhomogeneous strain profiles, generated, for example, by depositing TMDCs on pre-patterned substrates[188], can create a spatially varying bandgap in an initially homogeneous material, and can result in the appearance of the funnel effect, in which optically excited electron–hole pairs drift to areas of the sample where the bandgap is lower before recombining (FIG. 6c). This effect can be exploited to produce light-emitting devices that can be locally configured using strain[188].

The strain-induced modulation of electrical transport can be attributed mainly to the piezotronic and piezoresistive effects, which originate from the piezoelectric effect and from the strain-induced bandgap tuning in TMDCs, respectively. 2H polymorphs of 2D TMDCs with an odd number of layers are piezoelectric because of broken inversion symmetry[199,200]. Both the conversion of strain to voltage[201] and of voltage to strain (actuation)[186] have been reported for MoS_2. In this context, the piezotronic effect arises owing to piezoelectric polarization charges appearing at the sample edges, which increase or decrease the Schottky barrier height at the contact depending on the direction of the polarization field. Unlike the piezoelectric effect, the piezoresistive effect, which is due to the strain-induced modulation of the bandgap, appears both in odd and even-layered

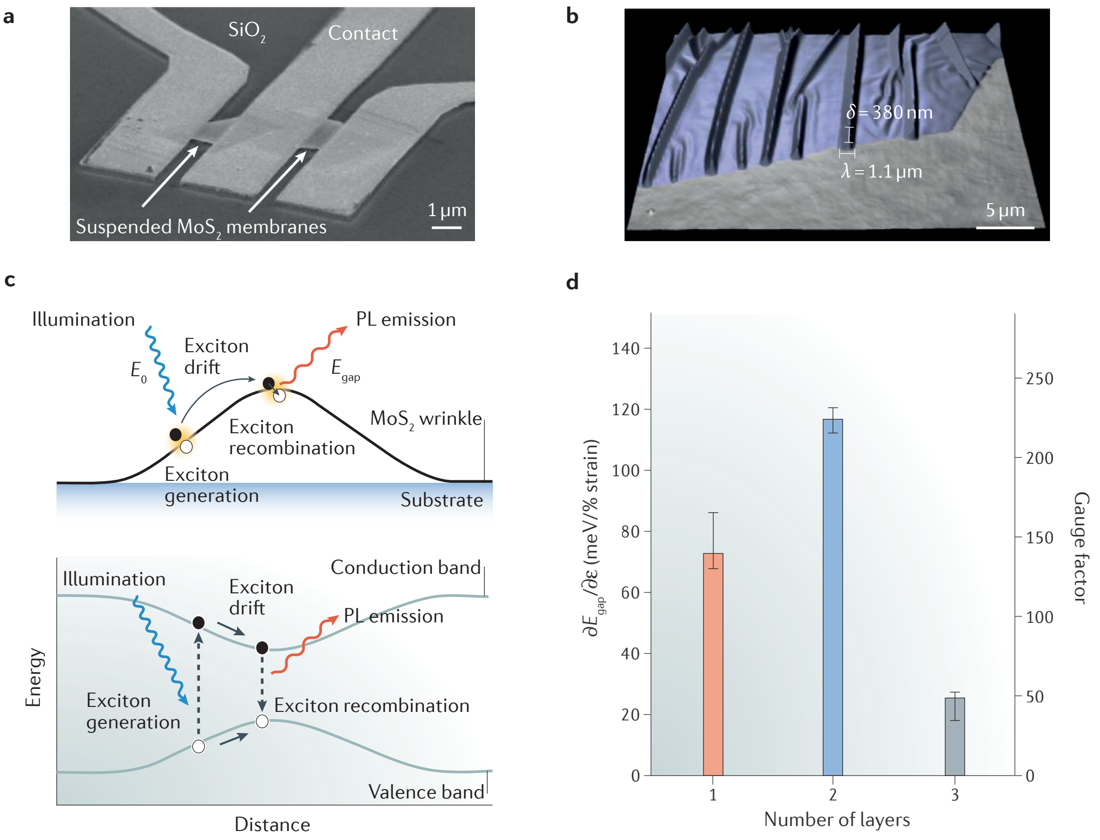

Figure 6 | **Strain engineering in TMDC-based devices. a** | Scanning electron microscope image of a device with a suspended MoS$_2$ channel; electrical contact electrodes clamp the suspended membrane. The suspension is achieved by wet-etching the underlying oxide substrate and ensures the mechanical degree of freedom required for applying strain using a probe. **b** | Three-dimensional rendering based on an atomic force microscope image of a wrinkled few-layer MoS$_2$ flake. An elastomeric substrate is stretched before the deposition of MoS$_2$. The strain is then released, producing a buckling-induced delamination of the MoS$_2$ flakes, which results in a localized strain profile. **c** | Schematic depiction of the funnel effect due to the localized strain profile in MoS$_2$. Owing to the application of local strain (top panel), the bandgap of the material is locally modified (bottom panel), giving rise to the funnel effect: excitons drift hundreds of nanometres to recombine in the regions of the sample with a lower bandgap. This results in the formation of areas exhibiting strain-induced localized emission. **d** | Strain-induced bandgap tuning and piezoresistivity due to mechanical deformation of the MoS$_2$ membrane for mono-, bi- and trilayer MoS$_2$ devices. The graph shows experimentally extracted values for the bandgap change rate and for the piezoresistive gauge factor. ε, strain; E_0, energy of incoming photon; E_{gap}, bandgap energy; PL, photoluminescence; TMDC, transition metal dichalcogenide. Panels **a** and **d** are adapted with permission from REF. 185, American Chemical Society. Panels **b** and **c** are adapted with permission from REF. 192, American Chemical Society.

atomically thin TMDCs. Electromechanical experiments on locally strained, suspended MoS$_2$, in which electrical conductivity measurements are performed in parallel with mechanical deformation applied using an atomic force microscope, can quantify the piezoresistive effect. The resulting gauge factors (the ratio of the relative change in electrical resistance to the strain) are greater than 100 for mono- and bilayer MoS$_2$ (REF. 185) (FIG. 6d). The piezoresitive coefficients for mono- and bilayer MoS$_2$ are comparable to those of state-of-the-art silicon strain sensors[202] and two orders of magnitude higher than that of graphene[203,204]. However, MoS$_2$ has a much higher fracture strain (as high as 11%)[160] than silicon (0.7%)[205], thus it would be more suitable for flexible strain sensors for use on curved surfaces and highly deformable objects, such as biological tissue. The presence of both piezoresistive and piezoelectric effects in MoS$_2$ makes this material a promising candidate for ultralow power piezoelectric transduction logic devices[206,207]. The exploitation of these effects has been demonstrated in MoS$_2$-based flexible photodetectors, in which the optical response could be modulated using piezophototronic effects[208].

The combination of high breaking strain and favourable electrical and optical properties makes 2D TMDCs highly promising materials for the realization of large-area, high-performance flexible devices and circuits. Research on flexible 2D TMDC devices started in 2012 and has achieved performances superior to those of organic, amorphous and metal oxide thin-film transistors. Learning from the experience with graphene, the top-gate device structure was avoided for flexible TMDC transistors[209–211], preventing the reduced yield and weaker performance caused by complications related to the fabrication of the gate stack on flexible substrates[212]. Instead, for TMDC thin-film transistors, the gate structures and channel regions were fabricated separately and transferred together later[213], or embedded gate structures[210,211] and ionic gel gating[209,214] were used. It is also important to note that the concept of flexible devices extends to stretchability in addition to bendability, making TMDCs particularly suitable for these applications. Stretching flexible TMDC transistors would allow piezoresistive strain sensing[215,216]. Recently, TMDC-based integrated circuits on flexible substrates were also realized[217].

Conclusions

We have summarized some of the recent key results on the electronic properties of 2D TMDCs, and in particular of MoS_2, which is the most studied TMDC material because of its robustness and the high availability of the raw material. Owing to their wide range of electrical properties, the atomic-scale thickness of their single layers and the possibility of obtaining a direct bandgap in semiconductor TMDCs, these materials display a rich physics and hold promise for a wide range of applications in low-power electronics, flexible electronics, optoelectronics, straintronics or spintronics. Furthermore, TMDCs show promise for biophysics applications, such as DNA sequencing and personalized medicine, because nanopores based on atomically thin membranes of TMDCs were shown to provide a rapid, high-resolution method for DNA sequencing. Although the atomic thickness of TMDC-based nanopores enables the necessary spatial resolution for nanopore DNA sequencing, the fast translocation speeds of DNA across such ultrathin membranes limits the detectability of single nucleotides. This issue has been addressed by using ionic liquids to create a viscosity gradient that can control the DNA translocation across MoS_2 nanopores[218,219].

The rapid progress of the field of TMDCs is reflected in the large number of scientists working on these materials and in the fast rise in the number of publications. However, the field is in many ways still in its early stage, with a large number of TMDC materials that have not been seriously studied or even synthesized yet and which promise many more exciting discoveries.

1. Radisavljevic, B., Radenovic, A., Brivio, J., Giacometti, V. & Kis, A. Single-layer MoS_2 transistors. *Nat. Nanotechnol.* **6**, 147–150 (2011).
2. Splendiani, A. *et al.* Emerging photoluminescence in monolayer MoS_2. *Nano Lett.* **10**, 1271–1275 (2010).
3. Mak, K. F., Lee, C., Hone, J., Shan, J. & Heinz, T. F. Atomically thin MoS_2: a new direct-gap semiconductor. *Phys. Rev. Lett.* **105**, 136805 (2010).
4. Dickinson, R. G. & Pauling, L. The crystal structure of molybdenite. *J. Am. Chem. Soc.* **45**, 1466–1471 (1923).
5. Wilson, J. A. & Yoffe, A. D. The transition metal dichalcogenides discussion and interpretation of the observed optical, electrical and structural properties. *Adv. Phys.* **18**, 193–335 (1969).
6. Frindt, R. F. & Yoffe, A. D. Physical properties of layer structures: optical properties and photoconductivity of thin crystals of molybdenum disulphide. *Proc. R. Soc. A* **273**, 69–83 (1963).
7. Joensen, P., Frindt, R. F. & Morrison, S. R. Single-layer MoS_2. *Mater. Res. Bull.* **21**, 457–461 (1986).
8. Tenne, R., Margulis, L., Genut, M. & Hodes, G. Polyhedral and cylindrical structures of tungsten disulfide. *Nature* **360**, 444–446 (1992).
9. Feldman, Y., Wasserman, E., Srolovitz, D. J. & Tenne, R. High-rate, gas-phase growth of MoS_2 nested inorganic fullerenes and nanotubes. *Science* **267**, 222–225 (1995).
10. Koppens, F. H. L. *et al.* Photodetectors based on graphene, other two-dimensional materials and hybrid systems. *Nat. Nanotechnol.* **9**, 780–793 (2014).
11. Xu, X., Yao, W., Xiao, D. & Heinz, T. F. Spin and pseudospins in layered transition metal dichalcogenides. *Nat. Phys.* **10**, 343–350 (2014).
12. Mak, K. F. & Shan, J. Photonics and optoelectronics of 2D semiconductor transition metal dichalcogenides. *Nat. Photonics* **10**, 216–226 (2016).
13. Hill, H. M., Rigosi, A. F., Rim, K. T., Flynn, G. W. & Heinz, T. F. Band alignment in MoS_2/WS_2 transition metal dichalcogenide heterostructures probed by scanning tunneling microscopy and spectroscopy. *Nano Lett.* **16**, 4837–4837 (2016).
14. Zhu, Z. Y., Cheng, Y. C. & Schwingenschlögl, U. Giant spin–orbit-induced spin splitting in two-dimensional transition-metal dichalcogenide semiconductors. *Phys. Rev. B* **84**, 153402 (2011).
15. Andor, K. *et al.* $k \cdot p$ theory for two-dimensional transition metal dichalcogenide semiconductors. *2D Mater.* **2**, 2053–1583 (2015).
16. Xiao, D., Liu, G.-B., Feng, W., Xu, X. & Yao, W. Coupled spin and valley physics in monolayers of MoS_2 and other group-VI dichalcogenides. *Phys. Rev. Lett.* **108**, 196802 (2012).
17. Pulkin, A. & Yazyev, O. V. Spin- and valley-polarized transport across line defects in monolayer MoS_2. *Phys. Rev. B* **93**, 041419 (2016).
18. Habe, T. & Koshino, M. Spin-dependent refraction at the atomic step of transition-metal dichalcogenides. *Phys. Rev. B* **91**, 201407 (2015).
19. Peierls, S. R. E. *Quantum Theory of Solids* (Clarendon Press, 1955).
20. Frohlich, H. On the theory of superconductivity: the one-dimensional case. *Proc. R. Soc. A* **223**, 305 (1954).
21. Chan, S.-K. & Heine, V. Spin density wave and soft phonon mode from nesting Fermi surfaces. *J. Phys. F Met. Phys.* **3**, 795–809 (1973).
22. Lomer, W. M. Electronic structure of chromium group metals. *Proc. Phys. Soc.* **80**, 489–496 (1962).
23. Wilson, J. A., Di Salvo, F. J. & Mahajan, S. Charge-density waves in metallic, layered, transition-metal dichalcogenides. *Phys. Rev. Lett.* **37**, C4-139-C4-150 (1974).
24. Wilson, J. A., Di Salvo, F. J. & Mahajan, S. Charge-density waves and superlattices in the metallic layered transition metal dichalcogenides. *Adv. Phys.* **50**, 1171–1248 (2010).
25. Moncton, D. E., Axe, J. D. & Di Salvo, F. J. Neutron scattering study of the charge-density wave transitions in $2H\text{-}TaSe_2$ and $2H\text{-}NbSe_2$. *Phys. Rev. B* **16**, 801–819 (1977).
26. Di Salvo, J., Francis, J. & Rice, T. M. Charge-density waves in transition-metal compounds. *Phys. Today* **32**, 32–38 (1979).
27. Revolinsky, E., Spiering, G. A. & Beerntsen, D. J. Superconductivity in the niobium–selenium system. *J. Phys. Chem. Solids* **26**, 1029–1034 (1965).
28. Perfetti, L., Gloor, T. A., Mila, F., Berger, H. & Grioni, M. Unexpected periodicity in the quasi-two-dimensional Mott insulator $1T\text{-}TaS_2$ revealed by angle-resolved photoemission. *Phys. Rev. B* **71**, 153101 (2005).
29. Sipos, B. *et al.* From Mott state to superconductivity in $1T\text{-}TaS_2$. *Nat. Mater.* **7**, 960–965 (2008).
30. Calandra, M. 2D materials: charge density waves go nano. *Nat. Nanotechnol.* **10**, 737–738 (2015).
31. Calandra, M., Mazin, I. I. & Mauri, F. Effect of dimensionality on the charge-density wave in few-layer $2H\text{-}NbSe_2$. *Phys. Rev. B* **80**, 241108 (2009).
32. Xi, X. *et al.* Strongly enhanced charge-density-wave order in monolayer $NbSe_2$. *Nat. Nanotechnol.* **10**, 765–769 (2015).
33. Ugeda, M. M. *et al.* Characterization of collective ground states in single-layer $NbSe_2$. *Nat. Phys.* **12**, 92–97 (2016).
34. Ge, Y. & Liu, A. Y. Effect of dimensionality and spin–orbit coupling on charge-density-wave transition in $2H\text{-}TaSe_2$. *Phys. Rev. B* **86**, 104101 (2012).
35. Yu, Y. *et al.* Gate-tunable phase transitions in thin flakes of $1T\text{-}TaS_2$. *Nat. Nanotechnol.* **10**, 270–276 (2015).
36. Hovden, R. *et al.* Atomic lattice disorder in charge-density-wave phases of exfoliated dichalcogenides ($1T\text{-}TaS_2$). *Proc. Natl Acad. Sci. USA* **113**, 11424 (2016).
37. Albertini, O. R. *et al.* Zone-center phonons of bulk, few-layer, and monolayer $1T\text{-}TaS_2$: detection of the commensurate charge density wave phase through Raman scattering. *Phys. Rev. B* **93**, 214109 (2016).
38. Sugawara, K. *et al.* Unconventional charge-density-wave transition in monolayer $1T\text{-}TiSe_2$. *ACS Nano* **10**, 1341–1345 (2016).
39. Chen, P. *et al.* Dimensional effects on the charge density waves in ultrathin films of $TiSe_2$. *Nano Lett.* **16**, 6331–6336 (2016).
40. Kohn, W. Excitonic phases. *Phys. Rev. Lett.* **19**, 439–442 (1967).
41. Jérome, D., Rice, T. M. & Kohn, W. Excitonic insulator. *Phys. Rev.* **158**, 462–475 (1967).
42. Guillamón, I. *et al.* Superconducting density of states and vortex cores of $2H\text{-}NbS_2$. *Phys. Rev. Lett.* **101**, 166407 (2008).
43. Valla, T. *et al.* Charge-density-wave-induced modifications to the quasiparticle self-energy in $2H\text{-}TaSe_2$. *Phys. Rev. Lett.* **85**, 4759–4762 (2000).
44. Nagata, S. *et al.* Superconductivity in the layered compound $2H\text{-}TaS_2$. *J. Phys. Chem. Solids* **53**, 1259–1263 (1992).
45. Freitas, D. C. *et al.* Strong enhancement of superconductivity at high pressures within the charge-density-wave states of $2H\text{-}TaS_2$ and $2H\text{-}TaSe_2$. *Phys. Rev. B* **93**, 184512 (2016).
46. Kusmartseva, A. F., Sipos, B., Berger, H., Forró, L. & Tutiš, E. Pressure induced superconductivity in pristine $1T\text{-}TiSe_2$. *Phys. Rev. Lett.* **103**, 236401 (2009).
47. Morosan, E. *et al.* Superconductivity in Cu_xTiSe_2. *Nat. Phys.* **2**, 544–550 (2006).
48. Wagner, K. E. *et al.* Tuning the charge density wave and superconductivity in Cu_xTaS_2. *Phys. Rev. B* **78**, 104520 (2008).
49. Yang, J. J. *et al.* Charge-orbital density wave and superconductivity in the strong spin-orbit coupled $IrTe_2$:Pd. *Phys. Rev. Lett.* **108**, 116402 (2012).
50. Kosterlitz, J. M. & Thouless, D. J. Ordering, metastability and phase transitions in two-dimensional systems. *J. Phys. C Solid State Phys.* **6**, 1181–1203 (1973).

51. Xi, X. *et al.* Ising pairing in superconducting NbSe$_2$ atomic layers. *Nat. Phys.* **12**, 139–143 (2016).
52. Lu, J. M. *et al.* Evidence for two-dimensional Ising superconductivity in gated MoS$_2$. *Science* **350**, 1353–1357 (2015).
53. He, W.-Y., Zhou, B. T., He, J. J., Zhang, T. & Law, K. T. Nodal topological superconductivity in monolayer NbSe$_2$. Preprint at *ArXiv* https://arxiv.org/abs/1604.02867 (2016).
54. Sharma, G. & Tewari, S. Yu-Shiba-Rusinov states and topological superconductivity in Ising paired superconductors. *Phys. Rev. B* **94**, 094515 (2016).
55. Zhou, B. T., Yuan, N. F. Q., Jiang, H.-L. & Law, K. T. Ising superconductivity and Majorana fermions in transition-metal dichalcogenides. *Phys. Rev. B* **93**, 180501 (2016).
56. Ye, J. T. *et al.* Superconducting dome in a gate-tuned band insulator. *Science* **338**, 1193–1196 (2012).
57. Costanzo, D., Jo, S., Berger, H. & Morpurgo, A. F. Gate-induced superconductivity in atomically thin MoS$_2$ crystals. *Nat. Nanotechnol.* **11**, 339–344 (2016).
58. Shi, W. *et al.* Superconductivity series in transition metal dichalcogenides by ionic gating. *Sci. Rep.* **5**, 12534 (2015).
59. Jo, S., Costanzo, D., Berger, H. & Morpurgo, A. F. Electrostatically induced superconductivity at the surface of WS$_2$. *Nano Lett.* **15**, 1197–1202 (2015).
60. Hasan, M. Z. & Kane, C. L. Colloquium: topological insulators. *Rev. Mod. Phys.* **82**, 3045–3067 (2010).
61. Qi, X.-L. & Zhang, S.-C. Topological insulators and superconductors. *Rev. Mod. Phys.* **83**, 1057–1110 (2011).
62. Qian, X., Liu, J., Fu, L. & Li, J. Quantum spin Hall effect in two-dimensional transition metal dichalcogenides. *Science* **346**, 1344–1347 (2014).
63. Bernevig, B. A., Hughes, T. L. & Zhang, S.-C. Quantum spin Hall effect and topological phase transition in HgTe quantum wells. *Science* **314**, 1757–1761 (2006).
64. Konig, M. *et al.* Quantum spin Hall insulator state in HgTe quantum wells. *Science* **318**, 766–770 (2007).
65. Knez, I., Du, R.-R. & Sullivan, G. Evidence for helical edge modes in inverted InAs/GaSb quantum wells. *Phys. Rev. Lett.* **107**, 136603 (2011).
66. Sabater, C. *et al.* Topologically protected quantum transport in locally exfoliated bismuth at room temperature. *Phys. Rev. Lett.* **110**, 176802 (2013).
67. Drozdov, I. K. *et al.* One-dimensional topological edge states of bismuth bilayers. *Nat. Phys.* **10**, 664–669 (2014).
68. Ali, M. N. *et al.* Large, non-saturating magnetoresistance in WTe$_2$. *Nature* **514**, 205–208 (2014).
69. Pletikosić, I., Ali, M. N., Fedorov, A. V., Cava, R. J. & Valla, T. Electronic structure basis for the extraordinary magnetoresistance in WTe$_2$. *Phys. Rev. Lett.* **113**, 216601 (2014).
70. Soluyanov, A. A. *et al.* Type-II Weyl semimetals. *Nature* **527**, 495–498 (2015).
71. Wang, Z. *et al.* MoTe$_2$: a type-II Weyl topological metal. *Phys. Rev. Lett.* **117**, 056805 (2016).
72. Sun, Y., Wu, S.-C., Ali, M. N., Felser, C. & Yan, B. Prediction of Weyl semimetal in orthorhombic MoTe$_2$. *Phys. Rev. B* **92**, 161107 (2015).
73. Bruno, F. Y. *et al.* Observation of large topologically trivial Fermi arcs in the candidate type-II Weyl semimetal WTe$_2$. *Phys. Rev. B* **94**, 121112 (2016).
74. Tamai, A. *et al.* Fermi arcs and their topological character in the candidate type-II Weyl semimetal MoTe$_2$. *Phys. Rev. X* **6**, 031021 (2016).
75. Huang, Y.-Preparation, S. Electrical and modulation optical properties of 2H-MoSe$_2$. *Chin. J. Phys.* **22**, 43–53 (1984).
76. Schäfer, H. *Chemical transport reactions.* (Academic Press, 1964).
77. Benameur, M. M. *et al.* Visibility of dichalcogenide nanolayers. *Nanotechnology* **22**, 125706 (2011).
78. Novoselov, K. S. *et al.* Two-dimensional atomic crystals. *Proc. Natl Acad. Sci. USA* **102**, 10451–10453 (2005).
79. Coleman, J. N. *et al.* Two-dimensional nanosheets produced by liquid exfoliation of layered materials. *Science* **331**, 568–571 (2011).
80. Nicolosi, V., Chhowalla, M., Kanatzidis, M. G., Strano, M. S. & Coleman, J. N. Liquid exfoliation of layered materials. *Science* **340**, 1226419 (2013).
81. Dines, M. B. Lithium intercalation via n-Butyllithium of the layered transition metal dichalcogenides. *Mater. Res. Bull.* **10**, 287–291 (1975).
82. Eda, G. *et al.* Photoluminescence from chemically exfoliated MoS$_2$. *Nano Lett.* **11**, 5111–5116 (2011).
83. Zeng, Z. *et al.* Single-layer semiconducting nanosheets: high-yield preparation and device fabrication. *Angew. Chem. Int. Ed.* **50**, 11093–11097 (2011).
84. Gordon, R. A., Yang, D., Crozier, E. D., Jiang, D. T. & Frindt, R. F. Structures of exfoliated single layers of WS$_2$, MoS$_2$, and MoSe$_2$ in aqueous suspension. *Phys. Rev. B* **65**, 125407 (2002).
85. Kappera, R. *et al.* Phase-engineered low-resistance contacts for ultrathin MoS$_2$ transistors. *Nat. Mater.* **13**, 1128–1134 (2014).
86. Joyce, B. A. Molecular beam epitaxy. *Rep. Prog. Phys.* **48**, 1637–1697 (1985).
87. Koma, A. & Yoshimura, K. Ultrasharp interfaces grown with van der waals epitaxy. *Surf. Sci.* **174**, 556–560 (1986).
88. Ohuchi, F. S., Shimada, T., Parkinson, B. A., Ueno, K. & Koma, A. Growth of MoSe$_2$ thin-films with Van der Waals epitaxy. *J. Cryst. Growth* **111**, 1033–1037 (1991).
89. Ohuchi, F. S., Parkinson, B. A., Ueno, K. & Koma, A. Van der Waals epitaxial growth and characterization of MoSe$_2$ thin films on SnS$_2$. *J. Appl. Phys.* **68**, 2168–2175 (1990).
90. Koma, A. Van der Waals epitaxy for highly lattice-mismatched systems. *J. Cryst. Growth* **201–202**, 236–241 (1999).
91. Dumcenco, D. *et al.* Large-area epitaxial monolayer MoS$_2$. *ACS Nano* **9**, 4611–4620 (2015).
92. Lehtinen, O. *et al.* Atomic scale microstructure and properties of Se-deficient two-dimensional MoSe$_2$. *ACS Nano* **9**, 3274–3283 (2015).
93. Roy, A. *et al.* Structural and electrical properties of MoTe$_2$ and MoSe$_2$ grown by molecular beam epitaxy. *ACS Appl. Mater. Interfaces* **8**, 7396–7402 (2016).
94. Ugeda, M. M. *et al.* Giant bandgap renormalization and excitonic effects in a monolayer transition metal dichalcogenide semiconductor. *Nat. Mater.* **13**, 1091–1095 (2014).
95. Barja, S. *et al.* Charge density wave order in 1D mirror twin boundaries of single-layer MoSe$_2$. *Nat. Phys.* **12**, 751–756 (2016).
96. Aretouli, K. E. *et al.* Epitaxial 2D SnSe$_2$/ 2D WSe$_2$ van der Waals heterostructures. *ACS Appl. Mater. Interfaces* **8**, 23222–23229 (2016).
97. Xenogiannopoulou, E. *et al.* High-quality, large-area MoSe$_2$ and MoSe$_2$/Bi$_2$Se$_3$ heterostructures on AlN(0001)/Si(111) substrates by molecular beam epitaxy. *Nanoscale* **7**, 7896–7905 (2015).
98. Vishwanath, S. *et al.* Comprehensive structural and optical characterization of MBE grown MoSe$_2$ on graphite, CaF2 and graphene. *2D Mater.* **2**, 024007 (2015).
99. Zhan, Y., Liu, Z., Najmaei, S., Ajayan, P. M. & Lou, J. Large-area vapor-phase growth and characterization of MoS$_2$ atomic layers on a SiO$_2$ substrate. *Small* **8**, 966–971 (2012).
100. Liu, K.-K. *et al.* Growth of large-area and highly crystalline MoS$_2$ thin layers on insulating substrates. *Nano Lett.* **12**, 1538–1544 (2012).
101. Shi, Y. *et al.* Van der Waals epitaxy of MoS$_2$ layers using graphene as growth templates. *Nano Lett.* **12**, 2784–2791 (2012).
102. Lee, Y.-H. *et al.* Synthesis of large-area MoS$_2$ atomic layers with chemical vapor deposition. *Adv. Mater.* **24**, 2320–2325 (2012).
103. Najmaei, S. *et al.* Vapor phase growth and grain boundary structure of molybdenum disulfide atomic layers. *Nat. Mater.* **12**, 754–759 (2013).
104. van der Zande, A. M. *et al.* Grains and grain boundaries in highly crystalline monolayer molybdenum disulphide. *Nat. Mater.* **12**, 554–561 (2013).
105. Zou, X., Liu, Y. & Yakobson, B. I. Predicting dislocations and grain boundaries in two-dimensional metal-disulfides from the first principles. *Nano Lett.* **13**, 253–258 (2012).
106. Najmaei, S. *et al.* Electrical transport properties of polycrystalline monolayer molybdenum disulfide. *ACS Nano* **8**, 7930–7937 (2014).
107. Chung, J.-W., Dai, Z. R. & Ohuchi, F. S. WS$_2$ thin films by metal organic chemical vapor deposition. *J. Cryst. Growth* **186**, 137–150 (1998).
108. Dumcenco, D. *et al.* Large-area MoS$_2$ grown using H$_2$S as the sulphur source. *2D Mater.* **2**, 044005 (2015).
109. Eichfeld, S. M. *et al.* Highly scalable, atomically thin WSe$_2$ grown via metal–organic chemical vapor deposition. *ACS Nano* **9**, 2080–2087 (2015).
110. Kang, K. *et al.* High-mobility three-atom-thick semiconducting films with wafer-scale homogeneity. *Nature* **520**, 656–660 (2015).
111. Wang, X. *et al.* Chemical vapor deposition growth of crystalline monolayer MoSe$_2$. *ACS Nano* **8**, 5125–5131 (2014).
112. Xia, J. *et al.* CVD synthesis of large-area, highly crystalline MoSe$_2$ atomic layers on diverse substrates and application to photodetectors. *Nanoscale* **6**, 8949–8955 (2014).
113. Chang, Y.-H. *et al.* Monolayer MoSe$_2$ grown by chemical vapor deposition for fast photodetection. *ACS Nano* **8**, 8582–8590 (2014).
114. Gao, Y. *et al.* Large-area synthesis of high-quality and uniform monolayer WS$_2$ on reusable Au foils. *Nat. Commun.* **6**, 8569 (2015).
115. Kobayashi, Y. *et al.* Growth and optical properties of high-quality monolayer WS$_2$ on graphite. *ACS Nano* **9**, 4056–4063 (2015).
116. McCreary, K. M., Hanbicki, A. T., Jernigan, G. G., Culbertson, J. C. & Jonker, B. T. Synthesis of large-area WS$_2$ monolayers with exceptional photoluminescence. *Sci. Rep.* **6**, 19159 (2016).
117. Okada, M. *et al.* Direct chemical vapor deposition growth of WS$_2$ atomic layers on hexagonal boron nitride. *ACS Nano* **8**, 8273–8277 (2014).
118. Tan, H. *et al.* Ultrathin 2D photodetectors utilizing chemical vapor deposition grown WS$_2$ with graphene electrodes. *ACS Nano* **10**, 7866–7873 (2016).
119. Tanabe, I. *et al.* Band structure characterization of WS$_2$ grown by chemical vapor deposition. *Appl. Phys. Lett.* **108**, 252103 (2016).
120. Zhang, Y. *et al.* Controlled growth of high-quality monolayer WS$_2$ layers on sapphire and imaging its grain boundary. *ACS Nano* **7**, 8963–8971 (2013).
121. Chen, J. *et al.* Chemical vapor deposition of large-sized hexagonal WSe$_2$ crystals on dielectric substrates. *Adv. Mater.* **27**, 6722–6727 (2015).
122. Liu, B. *et al.* Chemical vapor deposition growth of monolayer WSe$_2$ with tunable device characteristics and growth mechanism study. *ACS Nano* **9**, 6119–6127 (2015).
123. Yoshida, M. *et al.* Gate-optimized thermoelectric power factor in ultrathin WSe$_2$ single crystals. *Nano Lett.* **16**, 2061–2065 (2016).
124. Keyshar, K. *et al.* Chemical vapor deposition of monolayer rhenium disulfide (ReS$_2$). *Adv. Mater.* **27**, 4640–4648 (2015).
125. He, X. *et al.* Chemical vapor deposition of high-quality and atomically layered ReS$_2$. *Small* **11**, 5423–5429 (2015).
126. Hafeez, M., Gan, L., Li, H., Ma, Y. & Zhai, T. Large-area bilayer ReS$_2$ film/multilayer ReS$_2$ flakes synthesized by chemical vapor deposition for high performance photodetectors. *Adv. Funct. Mater.* **26**, 4551–4560 (2016).
127. Hafeez, M., Gan, L., Li, H., Ma, Y. & Zhai, T. Chemical vapor deposition synthesis of ultrathin hexagonal ReSe$_2$ flakes for anisotropic raman property and optoelectronic application. *Adv. Mater.* **28**, 8296–8301 (2016).
128. Naylor, C. H. *et al.* Monolayer single-crystal 1T′-MoTe$_2$ grown by chemical vapor deposition exhibits weak antilocalization effect. *Nano Lett.* **16**, 4297–4304 (2016).
129. Zhou, J. *et al.* Large-area and high-quality 2D transition metal telluride. *Adv. Mat.* **29**, 1603471 (2017).
130. Duan, X. *et al.* Lateral epitaxial growth of two-dimensional layered semiconductor heterojunctions. *Nat. Nanotechnol.* **9**, 1024–1030 (2014).
131. Huang, C. *et al.* Lateral heterojunctions within monolayer MoSe$_2$–WSe$_2$ semiconductors. *Nat. Mater.* **13**, 1096–1101 (2014).
132. Gong, Y. *et al.* Vertical and in-plane heterostructures from WS$_2$/MoS$_2$ monolayers. *Nat. Mater.* **13**, 1135–1142 (2014).
133. Li, M.-Y. *et al.* Epitaxial growth of a monolayer WSe$_2$–MoS$_2$ lateral p–n junction with an atomically sharp interface. *Science* **349**, 524–528 (2015).
134. Yu, H., Kutana, A. & Yakobson, B. I. Carrier delocalization in two-dimensional coplanar p–n junctions of graphene and metal dichalcogenides. *Nano Lett.* **16**, 5032–5036 (2016).
135. Kaasbjerg, K., Thygesen, K. S. & Jacobsen, K. W. Phonon-limited mobility in n-type single-layer MoS$_2$ from first principles. *Phys. Rev. B* **85**, 115317 (2012).
136. Kaasbjerg, K., Thygesen, K. S. & Jauho, A.-P. Acoustic phonon limited mobility in two-dimensional semiconductors: deformation potential and piezoelectric scattering in monolayer MoS$_2$ from first principles. *Phys. Rev. B* **87**, 235312 (2013).

137. Zhang, W., Huang, Z., Zhang, W. & Li, Y. Two-dimensional semiconductors with possible high room temperature mobility. *Nano Res.* **7**, 1731–1737 (2014).
138. Li, X. *et al.* Intrinsic electrical transport properties of monolayer silicene and MoS$_2$ from first principles. *Phys. Rev. B* **87**, 115418 (2013).
139. Ma, N. & Jena, D. Charge scattering and mobility in atomically thin semiconductors. *Phys. Rev. X* **4**, 011043 (2014).
140. Fivaz, R. & Mooser, E. Mobility of charge carriers in semiconducting layer structures. *Phys. Rev.* **163**, 743–755 (1967).
141. Radisavljevic, B. & Kis, A. Mobility engineering and a metal–insulator transition in monolayer MoS$_2$. *Nat. Mater.* **12**, 815–820 (2013).
142. Baugher, B. W. H., Churchill, H. O. H., Yang, Y. & Jarillo-Herrero, P. Intrinsic electronic transport properties of high-quality monolayer and bilayer MoS$_2$. *Nano Lett.* **13**, 4212–4216 (2013).
143. Yu, Z. *et al.* Realization of room-temperature phonon-limited carrier transport in monolayer MoS$_2$ by dielectric and carrier screening. *Adv. Mater.* **28**, 547–552 (2016).
144. Chamlagain, B. *et al.* Mobility improvement and temperature dependence in MoSe$_2$ field-effect transistors on parylene-c substrate. *ACS Nano* **8**, 5079–5088 (2014).
145. Cui, X. *et al.* Multi-terminal transport measurements of MoS$_2$ using a van der Waals heterostructure device platform. *Nat. Nanotechnol.* **10**, 534–540 (2015).
146. Bertolazzi, S., Krasnozhon, D. & Kis, A. Nonvolatile memory cells based on MoS$_2$/graphene heterostructures. *ACS Nano* **7**, 3246–3252 (2013).
147. Iqbal, M. W. *et al.* High-mobility and air-stable single-layer WS$_2$ field-effect transistors sandwiched between chemical vapor deposition-grown hexagonal BN films. *Sci. Rep.* **5**, 10699 (2015).
148. Xu, S. *et al.* Universal low-temperature Ohmic contacts for quantum transport in transition metal dichalcogenides. *2D Mater.* **3**, 021007 (2016).
149. Ovchinnikov, D., Allain, A., Huang, Y.-S., Dumcenco, D. & Kis, A. Electrical transport properties of single-layer WS$_2$. *ACS Nano* **8**, 8174–8181 (2014).
150. Fallahazad, B. *et al.* Shubnikov-de Haas oscillations of high-mobility holes in monolayer and bilayer WSe$_2$: Landau level degeneracy, effective mass, and negative compressibility. *Phys. Rev. Lett.* **116**, 086601 (2016).
151. Schwierz, F. Graphene transistors. *Nat. Nanotechnol.* **5**, 487–496 (2010).
152. Wu, Y. *et al.* State-of-the-art graphene high-frequency electronics. *Nano Lett.* **12**, 3062–3067(2012).
153. Yoon, Y., Ganapathi, K. & Salahuddin, S. How good can monolayer MoS$_2$ transistors be? *Nano Lett.* **11**, 3768–3773 (2011).
154. Krasnozhon, D., Lembke, D., Nyffeler, C., Leblebici, Y. & Kis, A. MoS$_2$ transistors operating at gigahertz frequencies. *Nano Lett.* **14**, 5905–5911 (2014).
155. Krasnozhon, D., Dutta, S., Nyffeler, C., Leblebici, Y. & Kis, A. High-frequency, scaled MoS$_2$ transistors. *IEEE Int. Electron Devices Meet.* http://dx.doi.org/10.1109/IEDM.2015.7409781 (2015).
156. Cheng, R. *et al.* Few-layer molybdenum disulfide transistors and circuits for high-speed flexible electronics. *Nat. Commun.* **5**, 5143 (2014).
157. Chang, H.-Y. *et al.* Large-area monolayer MoS$_2$ for flexible low-power RF nanoelectronics in the GHz regime. *Adv. Mater.* **28**, 1818–1823 (2015).
158. Sun, L. *et al.* 12-GHz thin-film transistors on transferrable silicon nanomembranes for high-performance flexible electronics. *Small* **6**, 2553–2557 (2010).
159. Wang, C. *et al.* Self-aligned, extremely high frequency III–V metal–oxide-semiconductor field-effect transistors on rigid and flexible substrates. *Nano Lett.* **12**, 4140–4145 (2012).
160. Bertolazzi, S., Brivio, J. & Kis, A. Stretching and breaking of ultrathin MoS$_2$. *ACS Nano* **5**, 9703–9709 (2011).
161. Ni, Z. H. *et al.* Uniaxial strain on graphene: raman spectroscopy study and band-gap opening. *ACS Nano* **2**, 2301–2305 (2008).
162. Pereira, V. M., Castro Neto, A. H. & Peres, N. M. R. Tight-binding approach to uniaxial strain in graphene. *Phys. Rev. B* **80**, 045401 (2009).
163. Johari, P. & Shenoy, V. B. Tuning the electronic properties of semiconducting transition metal dichalcogenides by applying mechanical strains. *ACS Nano* **6**, 5449–5456 (2012).
164. Yue, Q. *et al.* Mechanical and electronic properties of monolayer MoS$_2$ under elastic strain. *Phys. Lett. A* **376**, 1166–1170 (2012).
165. Shi, H., Pan, H., Zhang, Y.-W. & Yakobson, B. I. Quasiparticle band structures and optical properties of strained monolayer MoS$_2$ and WS$_2$. *Phys. Rev. B* **87**, 155304 (2013).
166. Dong, L., Namburu, R. R., O'Regan, T. P., Dubey, M. & Dongare, A. M. Theoretical study on strain-induced variations in electronic properties of monolayer MoS$_2$. *J. Mater. Sci.* **49**, 6762–6771 (2014).
167. Ghorbani-Asl, M., Borini, S., Kuc, A. & Heine, T. Strain-dependent modulation of conductivity in single-layer transition-metal dichalcogenides. *Phys. Rev. B* **87**, 235434 (2013).
168. Harada, N., Sato, S. & Yokoyama, N. Computational study on electrical properties of transition metal dichalcogenide field-effect transistors with strained channel. *J. Appl. Phys.* **115**, 034505 (2014).
169. Horzum, S. *et al.* Phonon softening and direct to indirect band gap crossover in strained single-layer MoSe$_2$. *Phys. Rev. B* **87**, 125415 (2013).
170. Lu, P., Wu, X., Guo, W. & Zeng, X. C. Strain-dependent electronic and magnetic properties of MoS$_2$ monolayer, bilayer, nanoribbons and nanotubes. *Phys. Chem. Chem. Phys.* **14**, 13035–13040 (2012).
171. Scalise, E., Houssa, M., Pourtois, G., Afanas'ev, V. V. & Stesmans, A. First-principles study of strained 2D MoS$_2$. *Phys. E* **56**, 416–421 (2014).
172. Wang, L., Kutana, A. & Yakobson, B. I. Many-body and spin–orbit effects on direct-indirect band gap transition of strained monolayer MoS$_2$ and WS$_2$: direct-indirect band gap transition in strained monolayer MoS$_2$ and WS$_2$. *Ann. Phys.* **526**, L7–L12 (2014).
173. Kumar, A. & Ahluwalia, P. K. Mechanical strain dependent electronic and dielectric properties of two-dimensional honeycomb structures of MoX$_2$ (X = S, Se, Te). *Phys. B (Amsterdam, Neth.)* **419**, 66–75 (2013).
174. Bhattacharyya, S., Pandey, T. & Singh, A. K. Effect of strain on electronic and thermoelectric properties of few layers to bulk MoS$_2$. *Nanotechnology* **25**, 465701 (2014).
175. Zhu, L. *et al.* Thermal conductivity of biaxial-strained MoS$_2$: sensitive strain dependence and size-dependent reduction rate. *Nanotechnology* **26**, 465707 (2015).
176. Rostami, H., Roldán, R., Cappelluti, E., Asgari, R. & Guinea, F. Theory of strain in single-layer transition metal dichalcogenides. *Phys. Rev. B* **92**, 195402 (2015).
177. Cheiwchanchamnangij, T., Lambrecht, W. R. L., Song, Y. & Dery, H. Strain effects on the spin–orbit-induced band structure splittings in monolayer MoS$_2$ and graphene. *Phys. Rev. B* **88**, 155404 (2013).
178. Koskinen, P., Fampiou, I. & Ramasubramaniam, A. Density-functional tight-binding simulations of curvature-controlled layer decoupling and band-gap tuning in bilayer MoS$_2$. *Phys. Rev. Lett.* **112**, 186802 (2014).
179. Sengupta, A., Ghosh, R. K. & Mahapatra, S. Performance analysis of strained monolayer MoS$_2$ MOSFET. *IEEE Trans. Electron. Devices* **60**, 2782–2787 (2013).
180. Mohammad Tabatabaei, S., Noei, M., Khaliji, K., Pourfath, M. & Fathipour, M. A first-principles study on the effect of biaxial strain on the ultimate performance of monolayer MoS$_2$-based double gate field effect transistor. *J. Appl. Phys.* **113**, 163708 (2013).
181. Feng, J., Qian, X., Huang, C.-W. & Li, J. Strain-engineered artificial atom as a broad-spectrum solar energy funnel. *Nat. Photonics* **6**, 866–872 (2012).
182. Kumar, H., Er, D., Dong, L., Li, J. & Shenoy, V. B. Elastic deformations in 2D van der waals heterostructures and their impact on optoelectronic properties: predictions from a multiscale computational approach. *Sci. Rep.* **5**, 10872 (2015).
183. Sharma, M., Kumar, A., Ahluwalia, P. K. & Pandey, R. Strain and electric field induced electronic properties of two-dimensional hybrid bilayers of transition-metal dichalcogenides. *J. Appl. Phys.* **116**, 063711 (2014).
184. Yu, S. *et al.* Strain-engineering the anisotropic electrical conductance in ReS$_2$ monolayer. *Appl. Phys. Lett.* **108**, 191901 (2016).
185. Manzeli, S., Allain, A., Ghadimi, A. & Kis, A. Piezoresistivity and strain-induced band gap tuning in atomically thin MoS$_2$. *Nano Lett.* **15**, 5330–5335 (2015).
186. Zhu, H. *et al.* Observation of piezoelectricity in free-standing monolayer MoS$_2$. *Nat. Nanotechnol.* **10**, 151–155 (2015).
187. Lloyd, D. *et al.* Band gap engineering with ultralarge biaxial strains in suspended monolayer MoS$_2$. *Nano Lett.* **16**, 5836–5841 (2016).
188. Li, H. *et al.* Optoelectronic crystal of artificial atoms in strain-textured molybdenum disulphide. *Nat. Commun.* **6**, 7381 (2015).
189. Conley, H. J. *et al.* Bandgap engineering of strained monolayer and bilayer MoS$_2$. *Nano Lett.* **13**, 3626–3630 (2013).
190. He, K., Poole, C., Mak, K. F. & Shan, J. Experimental demonstration of continuous electronic structure tuning via strain in atomically thin MoS$_2$. *Nano Lett.* **13**, 2931–2936 (2013).
191. Zhu, C. R. *et al.* Strain tuning of optical emission energy and polarization in monolayer and bilayer MoS$_2$. *Phys. Rev. B* **88**, 121301 (2013).
192. Castellanos-Gomez, A. *et al.* Local strain engineering in atomically thin MoS$_2$. *Nano Lett.* **13**, 5361–5366 (2013).
193. Plechinger, G. *et al.* Control of biaxial strain in single-layer molybdenite using local thermal expansion of the substrate. *2D Mater.* **2**, 015006 (2015).
194. Hui, Y. Y. *et al.* Exceptional tunability of band energy in a compressively strained trilayer MoS$_2$ sheet. *ACS Nano* **7**, 7126–7131 (2013).
195. Liu, Z. *et al.* Strain and structure heterogeneity in MoS$_2$ atomic layers grown by chemical vapour deposition. *Nat. Commun.* **5**, 5246 (2014).
196. Rice, C. *et al.* Raman-scattering measurements and first-principles calculations of strain-induced phonon shifts in monolayer MoS$_2$. *Phys. Rev. B* **87**, 081307 (2013).
197. Desai, S. B. *et al.* Strain-induced indirect to direct bandgap transition in multilayer WSe$_2$. *Nano Lett.* **14**, 4592–4597 (2014).
198. Island, J. O. *et al.* Precise and reversible band gap tuning in single-layer MoSe$_2$ by uniaxial strain. *Nanoscale* **8**, 2589–2593 (2016).
199. Duerloo, K.-A. N., Ong, M. T. & Reed, E. J. Intrinsic piezoelectricity in two-dimensional materials. *J. Phys. Chem. Lett.* **3**, 2871–2876 (2012).
200. Blonsky, M. N., Zhuang, H. L., Singh, A. K. & Hennig, R. G. Ab-initio prediction of piezoelectricity in two-dimensional materials. *ACS Nano* **9**, 9885–9891 (2015).
201. Wu, W. *et al.* Piezoelectricity of single-atomic-layer MoS$_2$ for energy conversion and piezotronics. *Nature* **514**, 470–474 (2014).
202. Kanda, Y. Piezoresistance effect of silicon. *Sens. Actuators Phys.* **28**, 83–91 (1991).
203. Smith, A. D. *et al.* Electromechanical piezoresistive sensing in suspended graphene membranes. *Nano Lett.* **13**, 3237–3242 (2013).
204. Huang, M., Pascal, T. A., Kim, H., Goddard, W. A. & Greer, J. R. Electronic—mechanical coupling in graphene from *in situ* nanoindentation experiments and multiscale atomistic simulations. *Nano Lett.* **11**, 1241–1246 (2011).
205. Petersen, K. E. Silicon as a mechanical material. *Proc. IEEE* **70**, 420–457 (1982).
206. Solomon, P. M. *et al.* Pathway to the piezoelectronic transduction logic device. *Nano Lett.* **15**, 2391–2395 (2015).
207. Newns, D., Elmegreen, B., Liu, X. H. & Martyna, G. A low-voltage high-speed electronic switch based on piezoelectric transduction. *J. Appl. Phys.* **111**, 084509 (2012).
208. Wu, W. *et al.* Piezophototronic effect in single-atomic-layer MoS$_2$ for strain-gated flexible optoelectronics. *Adv. Mater.* **28**, 8463–8468 (2016).
209. Pu, J. *et al.* Highly flexible MoS$_2$ thin-film transistors with ion gel dielectrics. *Nano Lett.* **12**, 4013–4017 (2012).
210. Chang, H.-Y. *et al.* High-performance, highly bendable MoS$_2$ transistors with high-K dielectrics for flexible low-power systems. *ACS Nano* **7**, 5446–5452 (2013).
211. Lee, G.-H. *et al.* Flexible and transparent MoS$_2$ field-effect transistors on hexagonal boron nitride-graphene heterostructures. *ACS Nano* **7**, 7931–7936 (2013).
212. Akinwande, D., Petrone, N. & Hone, J. Two-dimensional flexible nanoelectronics. *Nat. Commun.* **5**, 5678 (2014).
213. Yoon, J. *et al.* Highly flexible and transparent multilayer MoS$_2$ transistors with graphene electrodes. *Small* **9**, 3295–3300 (2013).
214. Pu, J. *et al.* Fabrication of stretchable MoS$_2$ thin-film transistors using elastic ion-gel gate dielectrics. *Appl. Phys. Lett.* **103**, 023505 (2013).

215. Shen, T., Penumatcha, A. V. & Appenzeller, J. Strain engineering for transition metal dichalcogenides based field effect transistors. *ACS Nano* **10**, 4712–4718 (2016).
216. Tsai, M.-Y. *et al.* Flexible MoS_2 field-effect transistors for gate-tunable piezoresistive strain sensors. *ACS Appl. Mater. Interfaces* **7**, 12850–12855 (2015).
217. Pu, J. *et al.* Highly flexible and high-performance complementary inverters of large-area transition metal dichalcogenide monolayers. *Adv. Mater.* **28**, 4111–4119 (2016).
218. Feng, J. *et al.* Identification of single nucleotides in MoS_2 nanopores. *Nat. Nanotechnol.* **10**, 1070–1076 (2015).
219. Feng, J. *et al.* Electrochemical reaction in single layer MoS_2: nanopores opened atom by atom. *Nano Lett.* **15**, 3431–3438 (2015).
220. Schmidt, H. *et al.* Transport properties of monolayer MoS_2 grown by chemical vapor deposition. *Nano Lett.* **14**, 1909–1913 (2014).

Acknowledgements
This work was financially supported by the European Research Council (Grant Nos. 682332 and 306504), Swiss National Science Foundation (Grant No. 153298), funding from the Single Nanometre Manufacturing project under the European Union's Seventh Framework Programme FP7/2007-2013 (Grant Agreement No. 318804), Marie Curie ITN network 'MoWSeS' (Grant No. 317451). We acknowledge funding by the European Commission under the Graphene Flagship (Grant Agreement No. 604391).

Competing interests statement
The authors declare no competing interests.

How to cite this article
Manzeli, S., Ovchinnikov, D., Pasquier, D., Yazyev, O. V. & Kis, A. 2D transition metal dichalcogenides. *Nat. Rev. Mater.* **2**, 17033 (2017).